Published in final edited form as:

NMR Biomed. 2023 June ; 36(6): e4671. doi:10.1002/nbm.4671.

CEST imaging of creatine, phosphocreatine, and protein arginine residue in tissues

Jiadi Xu[1,2,*], **Julius Juhyun Chung**[3], **Tao Jin**[3]

[1]F.M. Kirby Research Center for Functional Brain Imaging, Kennedy Krieger Research Institute, Baltimore, MD, USA

[2]Russell H. Morgan Department of Radiology and Radiological Science, The Johns Hopkins University School of Medicine, Baltimore, MD, USA

[3]Department of Radiology, University of Pittsburgh, Pittsburgh, Pennsylvania, USA

Abstract

Chemical exchange saturation transfer (CEST) MRI has become a promising technique to assay target proteins and metabolites through their exchangeable protons, noninvasively. The ubiquity of Creatine (Cr) and Phosphocreatine (PCr) due to their pivotal roles in energy homeostasis through the creatine phosphate pathway has made them prime targets for CEST in the diagnosis and monitoring of disease pathologies particularly in tissues heavily dependent on the maintenance of rich energy reserves. Guanidinium CEST from protein arginine residues, i.e. arginine CEST, can also provide information about the protein profile in tissue. However, numerous obfuscating factors stand as obstacles to the specificity of Arginine, Creatine and Phosphocreatine imaging through CEST such as semi-solid magnetization transfer (MT), fast chemical exchanges such as primary amines, and the effects of nuclear Overhauser enhancement (NOE) from aromatic and amide protons.

In this review, the specific exchange properties of protein Arginine residues, Cr and PCr along with their validation are discussed including the considerations necessary to target and tune their signal effects through CEST imaging. Additionally, strategies that have been employed to enhance the specificity of these exchanges in CEST imaging are described along with how they have opened up possible applications of protein Arginine residues, Cr and PCr CEST imaging in the study and diagnosis of pathology. A clear understanding of the capabilities and caveats of using CEST to image these vital metabolites and mitigation strategies is crucial to expanding the possibilities of this promising technology.

Keywords

Chemical Exchange Saturation Transfer (CEST); Creatine (Cr); Phosphocreatine (PCr); Arginine (Arg); Guanidinium (Guan); Magnetization Transfer

[*]**Corresponding Author:** Jiadi Xu, Ph.D., Kennedy Krieger Institute, The Johns Hopkins University School of Medicine, 707 N. Broadway, Baltimore, MD, 21205, xuj@kennedykrieger.org, Tel: 443-923-9572, Fax: 443-923-9505.

Introduction

Chemical exchange saturation transfer (CEST) MRI is a versatile technique that can significantly enhance the sensitivity of detecting low concentrations of proteins and metabolites through their exchangeable protons (1–8). Since the first discovery of the CEST phenomenon about two decades ago (9), this technique has been successfully applied to detect pathological chemical changes in many neurological and oncological diseases (10–21), as well as various metabolites in tissues (22–26). However, tissue contains many types of exchangeable protons with a diversity of exchanging rates on both sides of the Z-spectrum, such as the amide proton (10,27) in mobile proteins, amine protons from glutamate (Glu) at 3 ppm (14,24,25,28), amine protons from the lysine residues of proteins at 2.7–2.8 ppm, (24,29–32), guanidinium (Guan) protons from protein and creatine at 2 ppm, (16,33–38) the hydroxyl groups from proteins and myoinositol around 1 ppm (38–40), and the relayed nuclear Overhauser effect (NOE) signals from aliphatic protons in proteins and lipids between −4 and 0 ppm (23,39,41,42). The diversity of exchanging protons provides great opportunities for in vivo CEST applications, but also poses great challenges in extracting specific proton information. Among many endogenous CEST contrasts, amide protons (APT or amideCEST) (10,27) in mobile proteins with slow exchange rates of <100 s^{-1} (43,44) have been intensively studied due to their favorable properties, including high concentrations and large chemical shifts (3.5 ppm). These properties make the extraction of the amide proton group possible from the in vivo Z-spectrum by making use of its line-shapes. (37,45) Here, amideCEST indicates the CEST peak at 3.5 ppm to distinguish from APT which is usually obtained by asymmetry analysis at 3.5 ppm. Recently, guanidinium CEST from mobile protein and Creatine (Cr) were discovered and have drawn much attention (33–35,46). GuanCEST was initially studied in Cr molecules by Phillip Sun et. al. (47,48) and Mohammad Haris et. al.(46) In the initial Cr CEST study, the phantom pH was adjusted to slow down the exchange rate for use in amideCEST optimization (47,48). Recently, it was discovered that GuanCEST is also widely available in many kinds of proteins and brain Z-spectra at 2 ppm, which overlap with CrCEST and phosphocreatine (PCr) CEST signals.(33–37) In order to distinguish GuanCEST between proteins and Cr, the CEST peak at 2 ppm from Cr is referred to as CrCEST, while ArgCEST is used for protein GuanCEST since only Arg residues contain Guan groups in proteins. Although free Arg amino acids can contribute to the GuanCEST, this contribution is usually negligible due to the extremely low concentration of free Arg amino acids in tissues (<1 mM) compared to the Arg residues in the mobile proteins.(49) In PCr, the Guan group is phosphorylated and is separated to two peaks, i.e. PCrCEST (2.5 ppm) and PCrCEST(2 ppm). Similar to AmideCEST, PCrCEST also have relatively large chemical shifts (2 ppm and 2.5 ppm) and slow exchange rates (<200 s^{-1}), which leads to two distinguishable peaks at 2 or 2.5 ppm at high magnetic fields. Therefore, ArgCEST, CrCEST together with PCrCEST are the few CEST contrasts that can be extracted with high confidence from the crowded in vivo Z-spectrum. At 2 ppm, there are other CEST and NOE contrasts such as aromaticNOE, amineCEST and even hydroxylCEST. In the current review, we aim to summarize the components that include Guan or phosphorylated Guan groups comprising ArgCEST, CrCEST and PCrCEST. Other CEST/NOE components at 2 ppm are difficult to extract due to their broad line-shape and are not the topic of the current review. We will summarize the

validation of the ArgCEST, CrCEST and PCrCEST signals, as well as their acquisition and quantification. Finally, we will show some applications of ArgCEST, CrCEST and PCrCEST in assessing tumors, monitoring pH changes and Cr/PCr concentrations.

CrCEST, PCrCEST and ArgCEST signal validation

Phantom validation

As the first step of CEST experiments, the validation of CEST signals with phantoms can provide information about the chemical shifts and exchange rates of exchanging protons. CrCEST in phantoms was initially used for APT optimization at 3T. (47,48) Then, the feasibility of detecting PCr and Cr with CEST experiments was demonstrated on phantoms at both 9.4 T and 3 T. (46) In this study, it was confirmed that the Guan protons in Cr result in one single peak centered at 1.8 ppm with an exchange rate of 950 s^{-1}. The two amine groups in Guan are symmetric due to delocalization of the electron bonds due to resonance. As a result, the labile protons have the same chemical shift and are indistinguishable meaning they are modeled as a single exchange rate. The CrCEST at 3T MRI are plotted in Fig. 1a together with its molecular structure. CrCEST is in the intermediate exchange rate region at physical temperature 37°C for 3T and convalesce with water to form one broad peak. Therefore, it is very challenging to extract clean CrCEST signals at 3T for in vivo application. However, the CrCEST is a distinct single peak at high MRI fields as shown in Fig. 1d. A more detailed Cr exchange rate measurement was performed with water-exchange (WEX)-filtered ^{1}H NMR spectroscopy and found to be 1190 s^{-1} at 37 °C and pH 7.0. (50) The Cr exchange rates are strongly pH dependent. When pH decreased by 0.3 to 6.7, the exchange rate of Cr changes to 597 s^{-1}. In the same study, the deprotonation of the guanidinium group is also examined and found to be nearly zero, i.e. the average number n = (3.92±0.33) is close to 4 for the exchanging guanidinium protons per Cr molecule that contribute to the exchange process.

PCr contains two peaks resonating at 2.5 ppm and 1.8 ppm at 3T as shown in Fig. 1b. The exchange rates were found to be 140±60 s^{-1} (2.5 ppm) and 120±50 s^{-1} (1.8 ppm) at 37 °C and pH 7.0 in the original paper. (46) In one recent paper, the exchange rates were determined with a selective saturation recovery method and found to be 120±20 s^{-1} (2.5 ppm) and 78.7±10 s^{-1} (1.8 ppm) at 37°C and pH 7.0. (51) Similar to CrCEST, the exchange rates of PCrCEST are also strongly pH dependent. The exchange rates decreased to 67 s^{-1} (2.5 ppm) and 46 s^{-1} (1.8 ppm) at pH 6.7. The sensitivity of CrCEST is far higher than the amide protons of PCrCEST due to the higher proton number (4:2) and exchange rates (950 s^{-1} : 120 s^{-1}). In one comparison study on muscle at 11.7T MRI, the SNR gain using CEST is about 14.8 times higher than the proton MRS method for Cr, whereas for PCr it is about 2.4 times higher.(52) Therefore, many in vivo studies following the discovery of PCr and Cr CEST mainly focused on CrCEST.(53,54) However, CrCEST convalesces with water at 3T, which makes the extraction and quantification of CrCEST at low field very challenging. Recently, it was discovered that PCrCEST(2.5 ppm) is still individually distinguishable at 3T, which may be able to provide reliable quantitation of PCr. (51) In vivo PCr/Cr CEST will be further discussed in the following sections.

Proteins and peptides contain a diversity of exchanging protons in their side chains beside the backbone amide protons. Particularly Arg side chains have one guanidinium group, which overlap with Cr and PCr CEST signals. This is clearly demonstrated with the arginine-rich protein protamine (Fig. 1c).(33,55) A strong ArgCEST peak can be found at 2 ppm for the protamine Z-spectrum. When a saturation power of <1 μT is used, relatively faster exchanges like CrCEST signal will be inversely proportional to pH value, (56,57) which is different from slower exchange CEST contrasts. This type of inverse pH dependence has also been found in CEST imaging parameters targeting GluCEST (24) and mobile proteins (14), in which the range of exchange rates of interest (such as from 1200 s^{-1} to 500 s^{-1}) is faster than the Rabi frequency of the saturation pulses used (e.g., 400 rad/s for a 1.5 μT pulse).(33) ArgCEST is also commonly observable in many other proteins such as egg white (Figs. 1d and e). (34,37) In some early studies, GuanCEST sometime was considered CEST from amine protons, similar to the primary amine of glutamine and protein lysine residues, i.e. AmineCEST.(16,58) However, the center of AmineCEST of protein lysine residues is located at 2.7 ppm as revealed by the study on ischemic stroke (29,30) and egg white phantoms (57), while GluCEST is around 3 ppm. Also, because the linewidth of a CEST peak is approximately $\sqrt{\omega_1^2 + k_{ex}^2}$ (59), amineCEST has a broad lineshape and is only visible as one broad disguisable peak at low pH values at high fields.(14,60) Therefore, the sharp 2 ppm peak in the tissue Z-spectrum collected at high MRI fields is mainly a mixture of ArgCEST from protein and CrCEST as confirmed by the validation study on guanidinoacetate methyltransferase deficient ($GAMT^{-/-}$) mouse brain (35) and an ex vivo study using homogenous rat brain tissue (34). Beside the ArgCEST at 2 ppm, there are also strong amideNOE and aromaticNOE as demonstrated by the deuterium-hydrogen exchanging studies on model proteins (Fig. 1f). (37,61). In these studies, despite all chemical exchanging protons being replaced by deuterium atoms, strong amide and aromatic NOE signal was preserved at the positive offsets.

Validation of Cr, PCr and ArgCEST signal in tissue

Validation and optimization of the metabolic CEST signal in tissue Z-spectra is critical for its technique development. In the CEST field, however, few validation studies had been performed due to the challenge of varying the concentrations of the metabolite of interest while maintaining physiological conditions and other metabolic concentrations. PCr and Cr concentrations in tissues are stable and cannot be simply altered by intramuscular injection or intravenous infusion due to the Cr regulation by the creatine transporter. Since the discovery of CrCEST, the first in vivo validation was performed using different tumor models with different Cr concentrations.(17) The study suggests that the CEST peak at 2 ppm is correlated with Cr concentration, but there is still strong CEST from other components. However, the disadvantage of the method is that many other metabolites and proteins are altered with different tumor models. It is a challenge to quantify the exact contribution of CrCEST at 2 ppm. One *ex vivo* validation method has been proposed using dialysis to remove small molecules from tissue homogenates. (34) The study found there was still a strong signal (34 %) at 2 ppm in the dialyzed rat brain homogenates, i.e. Cr and PCr CEST contribute about 66 % signal at 2 ppm, with a saturation power of 1 μT as shown in Fig. 2a. Caution must be taken since *in vitro* MRI parameters such as T_1 and T_2 relativities are still significantly different from *in vivo* tissue, which may affect

the accuracy of the above conclusion. Recently, one creatine-deficient GAMT knockout ($GAMT^{-/-)}$ mouse model was generated. (35,52,62–64) GAMT is a key enzyme in the biosynthesis of Cr in the pancreas and liver. Without this enzyme, the biosynthesis of Cr will be terminated after the first step, i.e., transfer of the amidino group of arginine to glycine, to yield ornithine and guanidinoacetate (65). Then, the only source of Cr in the tissue of $GAMT^{-/-}$ mouse is through food. A creatine free diet was used to insure very low tissue total Cr and PCr concentrations (tCr).(35,52,62–64) Therefore, it is a perfect animal model to validate the specificity and sensitivity of Cr and PCr CEST. (35,52,66) It was found that the tCr contributed about 47% of the total signal at 2 ppm in mouse brain with 1 μT (2s) saturation power (Fig. 2b), which is close to the validation with in vitro rat brain homogenates (66%).(35) The tCr contribution increases as a function of saturation power, such that the tCr is about 80% with 2 μT (2s) saturation power. The same animal model can be also used to validate the PCr and Cr in the muscle and the results are presented in Fig. 2c. (52) Different from the brain, muscles contain a high concentration of PCr (~30 mM) and Cr (~10 mM). (67,68), where CrCEST is mostly observed at ~2 ppm and PCrCEST has been detected at 2 ppm and ~2.5–2.6 ppm. (69–71) Fig. 2c shows the comparison between the Z-spectra of the $GAMT^{-/-}$ and wild type (WT) mice with a saturation power of 1 μT. The Z-spectrum of the WT mice showed two clear peaks around 2 ppm and 2.5 ppm, while there was only one sharp peak around 2.2 ppm in the Z-spectrum of the $GAMT^{-/-}$ mice due to the high concentration of phosphate guanidinoacetate is present in $GAMT^{-/-}$ (62). Different from the brain, there was no visible protein ArgCEST peak in the skeletal muscle Z-spectrum (Fig. 2d), which allowed us to extract clean PCr and Cr CEST signals. PCrCEST was further investigated in animals after euthanasia because rapid dephosphorylation occurs postmortem, i.e. PCr converts to Cr rapidly as demonstrated by porcine (72) and mouse (73) postmortem studies. The Z-spectra of the mouse hindlimb are plotted in Fig. 2e. The PCr peak decreased significantly postmortem, exhibiting an 82.3 % drop (from 2.98 % to 0.52 %), and Cr exhibited a significant increase of approximately 90.6 % postmortem (from 3.86 % to 7.37 %). However, caution must be taken since postmortem studies suffer from the effects of concomitant physiological changes in pH, which affects exchange rates and thus CEST contrast, as well as from changes in concentration of other metabolites (e.g. lactate).

The validation of the ArgCEST signal in the brain Z-spectrum cannot be easily achieved by removing the mobile proteins in tissue similar to PCr/Cr CEST validation. However, we can exploit the property that CEST signals from arginine protons have strongly inverse pH-dependence at low saturation powers, whereas relayed NOEs have weak pH dependence and magnetization transfer contrast (MTC) is insensitive to pH (45,74) in the physiological range. As demonstrated by protein (Figs. 1c and e), the ArgCEST signal is visible with a peak around 2 ppm. However, there is still a large residual signal at 2 ppm that is not pH-dependent over the physiological range of pH 6.0 −7.5 (Fig. 1e). This conclusion is consistent with previous studies with animal stroke models at both high (29,33,45) (Fig. 2f) and low MRI fields (36) (Fig. 2g). Similar to the ArgCEST signal observed in protein phantoms (Figs. 1c and e), the ArgCEST signal was also found to be inversely dependent upon pH in the mouse brain. In addition to this, the background has contributions from NOEs, e.g. amideNOE and aromaticNOE. In order to show all the contributions between 2–2.5ppm in the Z-spectrum, the simulated brain Z-spectrum with GuanCEST, PCrCEST,

amideCEST, hydroxylCEST, amineCEST, amideNOE and aromaticNOE components are plotted in Fig. 3. The parameters used for simulating the Z-spectrum is listed in the Supplemental Materials. In summary, ArgCEST, PCrCEST and Cr CEST only contribute to the two peaks at 2 and 2.5–2.6 ppm in the tissue Z-spectrum. The large portion of this broad background signal between 2 and 2.5 ppm attributes faster exchanging protons from amine and hydroxyl groups, signals of which are partially merged with water due to being in the intermediate to fast exchange regime. Under typical saturation parameters used for slower exchanges (i.e., 0.5 to 2 uT), this portion of the CEST signal has low sensitivity and weak pH dependence in the physiological range (6–7.5).(57) In addition to this, the background between 2–2.5 ppm has contributions from nonCEST saturation transfer components including MTC, amideNOE and aromaticNOE. The NOE signals between 2–2.5 ppm were validated by hydrogen/deuterium (H/D) exchange studies (Fig. 1f). (37,61), and are attributable to aromatic protons, non-exchanging amide protons or amide protons with extremely slow exchange rates, which are still able to transfer magnetization to water following a two-step relayed NOE process with faster exchanging neighboring protons (42).

Acquisition of in vivo PCr/Cr/Arg CEST

Since the discovery of Cr/PCr CEST, it is generally recognized that Cr/PCr CEST was challenging to separate from other CEST components practically at low MRI fields such as 3T. Hence, acquisition parameters were optimized on phantoms in early CEST studies. However, in tissue CEST, it is known that the MTC effect from macromolecules can significantly alter optimal saturation power and length.(66) Recently, the polynomial fitting method was developed to extract Cr/PCr CEST signal from tissue Z-spectrum based on in vivo validation results. It allowed us to optimize the Cr/PCr acquisition parameters on tissue directly. In the following, we will discuss proper selection of saturation power and length for in vivo Arg/Cr/PCr CEST studies:

Saturation power selection

For CEST with intermediate and fast exchanging rates, the CEST signal is usually higher with stronger saturation power without MTC components as demonstrated in a phantom with Cr in solution (Figs. 4a). When strong MTC is present, such as *in vivo* CEST applications, the saturation power dependent CrCEST signal is totally different from those in solution. This can be illustrated by a phantom study with Cr in cross-linked bovine serum albumin (BSA) (Figs. 4b and 4c). CrCEST increases with saturation power initially (5 s saturation length), but drops rapidly when higher than 1 μT. Similar power dependent patterns were observed in some in vivo studies such as the muscle (Fig. 4d) (52) and brain (Fig. 4e) (35). The exchange rate of Cr in the brain is suggested to be lower than <1000 s^{-1} by a hypercapnia study on the animal brain. (75) The optimal saturation power (1 μT) for CrCEST was found to be 1–1.2 μT in both mouse brain and muscle indicating that Cr in cross-linked BSA phantoms can mimic the *in vivo* Cr situation well. The rapid CEST signal decay with high saturation powers when strong MTC present can be well explained by the scaling effect of the direct saturation (DS) and MTC effects following (35):

$$\Delta Z_{obs} = Z^{ss}_{back} 2(1 - Z_{clean}) \quad (1)$$

where $(1 - Z_{clean})$ is the clean CEST signal without MTC and DS, and ΔZ_{obs} is the observed CEST signal. For Arg/Cr/PCr CEST signals, with increasing power, saturation efficiency is proportional to the square of saturation power initially, and then levels off slowly until reaching a maximum saturation of one. However, MTC and DS keep increasing with increasing saturation powers, leading to an increase in Z_{back}^{ss}. As a result, the observed CEST signal will drop quickly at higher saturation power, as predicted in Eq. 1 and observations at both high (Figs. 4d and e) and low fields (Fig. 4h). Similar power and duration dependence has been reported in a previous study of amine-proton exchange.(14) The optimum saturation power for ArgCEST is around 0.8 μT at high field as measured by $GAMT^{-/-}$ mice without Cr/PCr in brain as shown in Fig. 4e (Green square). At lower MRI fields, DS causes a stronger scaling effect and leads to a slightly lower optimum saturation power (around 0.6 μT for PCrCEST) (Fig. 4h). Both CrCEST and ArgCEST do not show clearly distinguishable peaks at 3T and optimum saturation powers have not yet determined due to the difficulty of extracting a clean signal.

Saturation length selection

Conventionally, extremely long saturation lengths (> 3s) were chosen to reach steady-state saturation and to produce maximal CEST signal, particularly for preclinical scanners. Due to the hardware limitations of clinical MRI scanners, a relatively short saturation time (< 1s) is often used for human studies (76,77). The steady-state strategy is valid for CEST contrast without MTC, such as Cr solutions in Fig. 4b. However, this principle does not necessarily work for in vivo CEST when strong MTC and DS are present. With lower saturation powers (<1 μT), the CEST effect with respect to the saturation time is still approximated as a single exponential function.(78). On the contrary, CEST is a buildup and decay function for high saturation powers (>1 μT) as demonstrated by a Cr phantom mixed with cross linked BSA in Fig. 4f. When increasing saturation length, both the MTC background and the CEST saturation efficiency buildup exponentially, but the observed CEST signal is modulated by the scale-down effect following Eq. 1 due to MTC competition. Then, maximum observed CEST signal is reached at a saturation time slightly longer than $T_{1\rho}$, the rotation frame relaxation time at this saturation power, which is much shorter than the steady-state time, i.e., $5 \cdot T_{1\rho}$. This optimum saturation length that is much shorter than steady-state length has also been observed in amine proton studies using the chemical exchange-sensitive spin-lock (CESL) method with strong saturation powers (14,79).

In vivo CEST experiments

As we discussed above, it is common to see several exchanging protons at the same frequency offset for in vivo CEST, such as the ArgCEST and CrCEST at 2 ppm. The previous comparison study on the $GAMT^{-/-}$ and WT mice demonstrated that the ratio between ArgCEST and CrCEST is strongly power dependent.(66) Saturation power can be tuned to suppress contributions from unwanted exchanging protons, such that high powers can selectively enhance fast-exchanging components, while slow-exchanging CEST will be dominant with low saturation powers. Therefore, a saturation power of 2–3 μT was commonly used for CrCEST at both high and low fields instead of the optimum 0.6–1 μT.(29,53,54,66,80) However, high saturation power also causes severe scale-down effects due to MTC and DS (Eq.1), thus leading to much reduced Arg/Cr/PCr CEST signals. It is

necessary to point out that the above discussion focuses on conventional continuous wave or steady-state pulsed CEST methods. Arg, PCr and Cr CEST can be acquired with special editing techniques such as chemical exchange rotation transfer imaging (70). Considering Cr/PCr CEST signal is relatively low in tissue (<3%), the special editing further reduces CEST signal and will not be discussed in the current review.

Quantification of PCr/Cr/Arg Signal

In the early days of CEST development, most CEST signal was extracted using asymmetry analysis, i.e. CEST contrast was computed by subtracting the normalized magnetization signal at the frequency of interest, such as APT at 3.5 ppm and CrCEST at 1.8–2 ppm (3T) from the magnetization at the corresponding reference frequency symmetrically at the opposite side of the water resonance. (10,27,53,54) This method is demonstrated in the CrCEST maps on muscle in Figs. 5a and b. The MTC and DS were assumed to be symmetric around water resonance which would make them removable by this strategy. However, many studies showed that MTC is asymmetric around water resonance meaning background MTC would not be removed by asymmetry analysis.(81) There is also much evidence to suggest that many CEST signals from protein contribute to the resonance between 1–4 ppm such as amine and hydroxyl CEST from protein, (31) amideCEST and amideNOE (Fig. 3).(37) Furthermore, there are strong AliphaticNOE resonances that are centered at the opposite side of the water frequency and can contribute when performing asymmetry analyses (43,82–85). Therefore, the MTRasym at 1.8 ppm is a mixture of many CEST and NOE components. (Fig. 5b) With the recent validation studies in animal muscle, the maximum CrCEST signal in muscle is less than 3% with an optimum saturation power of 1 μT at high fields.(52,69) Although the MTRasym method can be used to study the Cr change relatively in tissue, the interference from other MRI parameters such as T_1, T_2 and pH variations due to the high signal from other CEST components must still be carefully considered.

In order to solve these issues faced by the MTRasym method, another strategy was developed in the CEST field named Lorentzian line-shape fitting. In this method as demonstrated in Figs. 5c and d, a full Z-spectrum was acquired with low saturation field strength B_1 and fit by assuming a Lorentzian line-shape for each contributing signal, such as DS, MTC, GuanCEST, amideCEST, amineCEST, and NOE peaks (16,17,86–88). This method can minimize the semi-solid macromolecule and DS components. However, it remains challenging to extract Arg/Cr/PCr CEST signal due to the difficulty of removing interference from amideNOE, aromaticNOE, amineCEST and hydroxylCEST that overlap with Arg/PCr/Cr CEST resonances as shown in Fig. 3. The CEST signal at 2 ppm extracted by Lorentzian fitting is still as high as 8% which includes CrCEST, ArgCEST, amineCEST, hydroxylCEST and aromaticNOE signals (Figs. 3 and 5d). The specificity of this method may be improved compared to MTRasym, but CrCEST is still less than 25% of the extracted CEST signal at 2 ppm.

From a previous validation study in animal muscle, it was found that Cr and PCr CEST have two discernible peaks at 2 or 2.5–2.6 ppm at high MRI fields. Therefore, Cr and PCr CEST can be extracted with localized Lorentzian fitting methods (Figs. 5e and f).(35,52,69)

In order to distinguish the method from the conventional Lorentzian fitting methods, this method is named the polynomial and Lorentzian line-shape Fitting (PLOF) approach and the procedure of the method is plotted in Figs. 5g–j. (35,52,66) PLOF fitting can be achieved by fitting the Z-spectrum directly. Another way is to convert the normalized Z-spectral intensity Z^{SS} to the longitudinal relaxation rate in the rotating frame, $R_{1\rho}$, i.e., the rotating-frame relaxation spectrum (R-spectrum) following (89–92)

$$Z(R_{1\rho}) = \left(1 - \frac{cos^2\theta R_1}{R_{1\rho}}\right)e^{-R_{1\rho}t_{sat}} + \frac{cos^2\theta R_1}{R_{1\rho}} \quad (2)$$

$R_1 = 1/T_1$ is the longitudinal relaxation rate of water, t_{sat} is the saturation time and θ is the tilt angle of the effective magnetization with respect to the Z-axis. $R_{1\rho}$ is the water relaxation rate in the rotating frame during saturation, which includes contributions from the effective water relaxation rate R_{eff}, the rotating frame rate from the CEST signal of interest (R_{exch}), and a term R_{back} that accounts for the rotating frame rates of all other magnetization/exchange transfer processes in tissue (91):

$$R_{1\rho} = R_{eff} + R_{back} + R_{exch} \quad (3)$$

where R_{eff} is the longitudinal relaxation rate of water in the rotating frame without additional solution components. The reason to convert the Z-spectrum to the rotating frame spectrum is that in the rotating frame all exchanging components including water direct saturation can be simply superimposed with respect to $R_{1\rho}$, while this is not feasible using a simple Z-spectrum. Therefore, the R spectrum can correct the scaling effect due to magnetization transfer and T_1 inhomogeneities in tissue (48,49). The observed CEST signal ΔZ is extracted by the following:

$$\Delta Z = Z(R_{eff} + R_{back}) - Z(R_{eff} + R_{back} + R_{exch}) \quad (4)$$

The CEST peak (R) and broad background (R_{back}) in the R-spectrum can be represented by a Lorentzian function and a mixed polynomial and Lorentzian function, respectively:

$$R = R_{exch}\frac{(w/2)^2}{(w/2)^2 + (\Delta\omega - \Delta\omega_{exch})^2} \quad (5)$$

$$R_{back} = \frac{C_0(C_1/2)^2}{(C_1/2)^2 + \Delta\omega^2} + C_2 + C_3 \cdot \Delta\omega \quad (6)$$

where w is the peak full-width-at-half-maximum (FWHM) of the Lorentzian line-shape. Δω is the offset relative to the water proton resonance. R_{exch} is the intensity of the CEST peak in the R-spectrum. $\Delta\omega_{exch}$ is the chemical shift offset of the CEST peak relative to the water signal, that is, 2.5 ppm for PCrCEST and 2 ppm for Cr/ArgCEST; The background function was modified from the original polynomial function (35,52,66) to improve PLOF background fitting for peaks close to the water resonance, i.e. Arg/PCr/Cr peaks. For amideCEST which is far from water resonant frequency, a simple polynomial function

can be used in Eq.6. (35,52,66) Lastly, the extracted CEST peaks expressed in R_{exch} are calibrated with metabolic or protein concentrations measured by ^{31}P or ^{1}H MRS and give the final Arg/PCr/Cr maps. In some special applications where the temporal resolution is critical, then the three-point method can be used. (69) The three-point method can be treated as a simplified PLOF method with the assumption that the background function Eq.6 is a linear function. Hence, it must be noted that this method only works for high fields with CEST offsets far away from water and low saturation powers. The three-point method also has high requirements on B0 homogeneity.

Artificial neural networks (ANNs) as a power pattern recognition tool are increasingly being used at many MRI fields (93–95) to extract relevant features from extremely large, annotated data sets. Once trained, ANNs can apply the learned knowledge to analyses of other data and/or solve task-specific problems. The ANN based CEST method was first demonstrated for mapping CEST contrasts between different fields (58) and extracting amideCEST and aliphaticNOE contrasts (96), i.e. deep learning CEST (deepCEST). In order to extract protein or metabolite concentrations directly from the Z-spectra recorded with CEST MRI, one ANNCEST method was developed and was demonstrated on phosphocreatine mapping in human muscle. (51) The ANNCEST will bypass the complicated conventional extraction and quantitation steps and link the concentration to the final Z-spectrum directly (Fig. 6a). Furthermore, ANNCEST can correct many errors introduced by B_0/B_1 inhomogeneity without performing B_1 and B_0 mapping. (Fig. 6b–f) The ANN is inherently suitable for CEST quantification: trained neural networks can efficiently and simultaneously predict multiple important properties, including metabolite concentration, the exchange rate of exchangeable protons, and B_1/B_0 related information, with just a simple input of a Z-spectrum for each voxel (Fig. 6b). The encoding process of CEST MRI can be well described by the Bloch-McConnell equations and a training Z-spectrum can be easily generated with known parameters. However, due to the complexity of the Bloch-McConnell equations, an accurate solution is hard to derive especially with the presence of possible B_0 and B_1 effects, which means decoding quantitative concentrations and exchange rates from Z-spectra can be challenging. Here, ANNCEST provides a new dimension for CEST quantification by directly linking the Z-spectrum with the quantitative parameters with an ANN network. However, the application of the ANNCEST method to extract Arg/Cr/PCr CEST in brain is far more complicated than in muscle. There are several components within brain tissue with significantly different MRI parameters such as white matter (WM), gray matter (GM) and cerebrospinal fluid (CSF). The advantages, disadvantages, and typical applications of the CEST quantification methods mentioned above are summarized in Tab. 1.

Applications of Arg/Cr/PCr CEST

Arg and Cr CEST for tumor assessment

ArgCEST detects the arginine rich protein content in tissue, while CrCEST reflects the creatine kinase reaction-based bioenergy status. Therefore, both can be used to assess the cellular chemistry and pathologic alterations in tumors. (16,17) Usually, the two signals are difficult to separate and were referred to collectively as a summed signal, GuanCEST. The first application of GuanCEST on tumor was demonstrated on the invasive murine cell-line

Lewis lung carcinoma (LLC) implanted in the mouse hind limb (Fig. 7a). The CEST(2 ppm) maps were extracted following the Lorentzian fitting method demonstrated in Figs. 4c and d. (16) Although, it was referred to as amineCEST at the time of the study, the signal at 2 ppm extracted with Lorentzian fitting is a mixed signal resulting from GuanCEST, amineCEST, hydroxylCEST, amideNOE and aromaticNOE signals as discussed above (Fig.3). Here, we refer to it as CEST(2 ppm) to represent the signal at 2 ppm extracted with Lorentzian fitting. It can be seen that the CEST(2 ppm) trends towards higher amplitudes as the tumor grows. The same method was further demonstrated in the rat brain implanted with tumor cells (9L gliosarcoma) (Fig. 7b&c). (17,97) Different from the LLC tumor, the CEST(2 ppm) for the 9L tumor decreases as the tumor grows. The difference may be due to the slightly higher saturation power (1μT), which introduced higher CrCEST contributions. CEST(2 ppm) was also demonstrated on human tumor patients at 9.4T (Fig. 7d) together with CEST(3.5 ppm) and aliphaticNOE. (58) The signal was also extracted with the Lorentzian fitting approach from the Z-spectrum acquired with 0.6 μT saturation power. Here, CEST(3.5ppm) is a mixture of amideCEST, amideNOE and amineCEST (Fig. 3), and also is different from APT which is obtained by asymmetry analysis. The CEST(3.5 ppm) shows hyperintensity in the tumor while aliphaticNOE maps show a clear decrease in the tumor area as well as a strong drop in the necrotic cyst. The CEST(2 ppm) signal shows less contrast than CEST(3.5 ppm), yet reveals similar hyperintensities in the tumor area. Note that T_1 and MTC often change in tumors which would affect the CEST contrast. This effect was not removed in some of the previous studies, therefore, some of the contrast may be due to these confounding effects. An $R_{1\rho}$-based analysis method such as AREX would improve the specificity of CrCEST and ArgCEST, as we discussed above. For tumor assessment, we do not need to separate particular CEST contrasts. The protein profiling provided by the MTasym or Lorentizan fitting at 2 ppm can provide information about tumor grading or differentiation between glioma and radiation necrosis similar to APT (27,98). However, if we aim to detect the microenviroment, such as pH and PCr/Cr energy metabolism, it is better to extract the particular contrast since it is difficult to determine the components obtained with MTasym or Lorientizan fitting. Since the protein content also changes in the tumor, it is more reliable to determine the microenviroment by extracting several CEST contrasts simultaneously such as AmideCEST, ArgCEST and CrCEST. Recent studies revealed that mitochondria in cancer cells show active function of oxidative phosphorylation (99). PCr/Cr mapping has great potential in being a non-invasive technique capable of providing additional information about tumor grading, treatment response and even advancing basic cancer biochemistry research.

pH mapping by Guan and PCrCEST

The homeostasis of tissue pH is essential for normal cellular functions and plays a vital role in cell physiology. Transient fluctuation of local brain pH has been observed during neuronal activation, seizure and spreading depression. Many pathophysiological processes, such as ischemic stroke, epilepsy, and traumatic brain injury can also introduce pH alterations. Thus, a non-invasive pH-sensitive imaging tool that can provide unique insight into the brain function and neurological disorders is desirable. (33,100) Most intracerebral pH probing techniques are highly invasive such as electrochemical (101), photoelectrochemical (102), optical imaging (103) and implantable pH micro sensors. On the other hand,

magnetic resonance spectroscopy (MRS) and its branches, such as ^{31}P MRS (104–106) or ^{1}H MRS after administration of agents (107–110), are well-established methods for non-invasively detecting pH changes in tissue. However, additional hardware requirements and limited accessibility hamper ^{31}P-wide clinical applications, while administration of agents is expensive and always comes with a risk. In addition, compared to MRI, MRS-based methods suffer from reduced detection sensitivity and a consequently lower spatial resolution.

CEST contrast is sensitive to both pH and metabolite/protein concentration. Therefore, both ArgCEST and CrCEST can be used for pH mapping. The pH change in most pathophysiological processes are very small on the order of <0.5 pH. Therefore, the pH sensitivity should be high enough to detect at least a 0.2 level of pH variation. The most important consideration in pH mapping with CEST is to suppress the NOE or MTC component that is not sensitive to pH change. This can be achieved by MTasym, three-point or PLOF fitting methods detailed in the sections above. However, the CEST components extracted with Lorentzian fitting still contains a large portion of NOE signals, which leads to compromise in pH sensitivity as demonstrated by recent comparison studies. (56,111) Considering that Cr concentrations are highly stable in the brain, around 5 mM in both mouse and rat (35,66), CrCEST is very suitable for pH mapping in the brain. In practice, the two contrasts are difficult to separate completely. Hence, the pH mapping on the brain was usually achieved with GuanCEST, i.e. the combined CEST contrasts from both ArgCEST and CrCEST. Also, it is not necessary to separate them for in vivo pH mapping since both contrasts are strongly dependent on pH. RF power-based ratiometric CEST imaging has been proposed for pH imaging. With these methods ratios of CEST effects obtained under different RF power levels have been compared with their pH dependence in CrCEST phantom studies.(112) This pH mapping method can be applied to in vivo tissue if the MTC and DS effects can be effectively removed by other quantitative methods such as multi-Lorentzian fitting.

In the CEST field, amideCEST or APT was the first CEST contrast used for pH mapping in the brain.(10,12) Here, APT is used for the CEST contrast at 3.5–3.6 ppm extracted with conventional MTRasym method, which is a mixed signal comprising amideCEST, amideNOE, amineCEST and aliphaticNOE.(37) Although it is in and of itself a mixed signal, it also works well in delineating ischemic regions by suppressing the majority of NOE and MTC components (111). Up to now, APT or amideCEST is still the most popular CEST contrast for pH mapping due to the abundance of amide protons in tissue. Although, amideCEST/APT MRI has been successful in measuring the pH change in acute ischemia and other diseases (18,29,46,50,53,113), the relatively slow exchange rate of amide protons ($<100\ s^{-1}$) at physiological temperature and pH limits its sensitivity in detecting subtle pH changes. GuanCEST can be a useful supplemental contrast for the commonly used APT in pH mapping.(29,56) When saturation power lies between the optimal powers for amides and creatine (< 1 μT), CrCEST signal increases with respect to the lower pH values.(56) Then, one strategy to enhance the sensitivity of pH mapping with CEST is using the two contrasts simultaneously, amideCEST and GuanCEST. The new contrast has been named pH_{enh} by acquiring both amide- and GuanCEST images, and subtracting them as

$$pH_{enh} = [S_{sat}(\alpha \times B_1, 3.6\ ppm) - S_{sat}(B_1, 2.0\ ppm)] \quad (7)$$

where α is the ratio of radio frequency powers for saturation at offsets 3.6 ppm and 2.0 ppm. The sensitivity of the pH_{enh} and APTw maps were demonstrated in stroke rats (Figs. 8a–d). pH_{enh} was obtained from GuanCEST at 2.0 ppm acquired with 30 Hz (0.7 μT) and amideCEST at 3.6 ppm with 54 Hz (1.26 μT). Both pH_{enh} and APTw map show a negative baseline due to NOE and asymmetric MTC effects. Tissue acidification appears hyperintense in pH_{enh} maps, while the same regions appear hypointense on APTw maps. The ischemic lesion can be well identified by pH_{enh} maps and is closely match with the ADC deficit. The contrast to noise ratio of pH_{enh} is about 2.9±0.4 times higher than APTw (Fig. 8d).

Different from low saturation powers for GuanCEST, (33,36,56,57) GuanCEST for pH mapping can be achieved with high saturation powers, in which the GuanCEST signal is reduced with lower pH values. (29,75) The reason for the totally different pH dependence of GuanCEST with low and high saturation powers is still not fully understood. The high sensitivity of GuanCEST for pH mapping with high powers was first demonstrated on the mouse brain with an ischemic stroke model. (29) Hypercapnia will cause a reduction in cerebral intracellular pH (114). To evaluate the sensitivity of GuanCEST in detecting pH change, CEST Z-spectra on wild type (WT) mouse brains pre- and post-20% CO_2 inhalation were recorded. There is need to be aware that while the signal was denoted CrCEST in the original study, (29,75) as we discussed above, the signal contains both Arg and CrCEST and should be named collectively as GuanCEST. GuanCEST showed better detection sensitivity than amideCEST (Figs. 8e–i). (75) One recent study showed a discovery that cerebral pH detected by GuanCEST is reduced in AD mice versus wild type (WT) mice. The typical GuanCEST Z-spectra and maps for the WT, Tau and APP^{swe}:PS1ΔE9 (APP) mouse brain are plotted in Figs. 8k&l. In this study, the apparent relaxation rate of Guan (R_{Guan}) was calculated with the PLOF method to correct for interference of the semi-solid magnetization transfer effect and T_1. Compared to WT GuanCEST maps, reduced GuanCEST intensities were observed in the Tau and APP mouse brains, especially in the cortical regions (WT: 0.105±0.017 s^{-1}; Tau: 0.084±0.083 s^{-1}; APP: 0.074±0.019 s^{-1}). A significant difference was obtained between WT and the Tau and APP GuanCEST in the cortex and corpus callosum regions ($p<0.01$) from regional values. Because the concentrations of Cr are the same in these mice models as validated by the ^1H and ^{31}P in the same study, these findings show potential to allow the measurement of pH change in the brain and to detect the presence of neurogenerative disease. In skeletal muscle, the abundance of PCr and Cr makes pH mapping possible by combining measurement of PCrCEST and CrCEST. A recent study by Chen et al (71) measured PCrCEST at 2.6 ppm and CrCEST at 2 ppm by multi-Lorentzian fitting at 7 T. A ratiometric analysis was used to remove the T_1 effect and determined a quantitative pH value using phantom calibration. Note that the application of this pH-mapping method in disease study would assume that there is negligible change in the relative concentration of PCr and Cr. If this assumption is not valid, it may be necessary to acquire data with multiple saturation powers to mitigate this problem.

Creatine kinase reaction measurement—Cr and PCr are two primary components of the creatine kinase reaction (CK) (115,116), whereby Cr is phosphorylated to PCr to form

an easy to mobilize reserve of high-energy phosphates (117). Therefore, quantification of the concentrations and tissue distribution of Cr and PCr are important for understanding cellular chemistry and assessing pathologic alterations. ^{1}H and ^{31}P magnetic resonance spectroscopy (MRS) are two major techniques to quantify tissue Cr and PCr concentrations. ^{1}H MRS can measure the total Cr (tCr), which is composed of Cr and PCr (118,119). In contrast, ^{31}P MRS is only capable of detecting PCr since Cr does not contain phosphorus (120,121). Similar to pH mapping, MRS quantification is limited by relatively low signal-to-noise ratio and spatial resolution. Here the Cr and PCr CEST methods enable us to measure Cr and PCr concentrations in tissues and hence CK function by performing plantar flexion exercise in the MRI scanner. The first CK measurement was performed by Reddy's group with CrCEST that extracted CEST signals with asymmetry analysis. (53,54,122) Plantar flexion exercise led to an increase in the CrCEST in all subjects. Fig. 9a shows CrCEST maps for the same subject before and after mild plantar flexion exercise with a temporal resolution of 24 s. The time dependence of the mean CrCEST for each segmented muscle group is plotted in Fig. 9b. The principal muscles involved in plantar flexion are located in the posterior compartment of the leg and include the soleus muscle as well as the medial (MG) and lateral (LG) heads of the gastrocnemius muscles. The CrCEST maps appeared fairly uniform at baseline while the first postexercise map showed a 6.7% and 7.2% increase in CrCEST in the LG and MG, respectively, following exercise. The CrCEST in all the muscles was seen to recover exponentially back to baseline after roughly three time points or about 2 min.

PCr shows one distinguishable peak with signal of about 0.8–1% of water signal in the Z-spectrum at 3T due to its much lower exchange rate ($260 \pm 40\ s^{-1}$), which provides a great opportunity to extract PCr concentrations with PLOF or ANNCEST. (51) The CK measurement with ANNCEST based PCr mapping was validated through measurement during in-magnet plantar flexion exercise (Figs. 9c–e). Shortly after exercise, the PCr depletion in the gastrocnemius muscles recovered to basal values on the PCr maps obtained by PCr ANNCEST as shown by the representative results in Figs. 9d. The spatially resolved map of the PCr recovery rate constant using ANNCEST is shown in Fig. 9e and a recovery time constant of 70.7±55.4 s was obtained, which is consistent with that reported in a previous study (63.1 ± 25.9 s)(123). The PCr depletion observed in the muscle regions is in good agreement with those reported previously in healthy volunteers using ^{31}P MRS, in which the gastrocnemius muscle showed significantly greater PCr depletion than other muscle groups during plantar flexion exercise (124–126).

CrCEST maps obtained by MTasym work well in determining relative Cr concentration changes. The high temporal resolution provided by MTasym is also helpful in revealing CK function, which usually occurs in a few minutes (123). Consideration must be taken for the fact that pH, T_1 and T_2 also change in the muscle during exercise (127–129). These effects can not be easily separated and accounted for by the MTasym method. A more reliable way to study the CK process would be to obtain the PCr and Cr CEST contrasts simultaneously to monitor the conversion from PCr to Cr. However, this extends the total experimental time significantly. Rapid MRI acquisition development is needed to properly implement this strategy. Similar to ^{31}P MRS, Cr/PCr CEST can be used for the noninvasive assessment of mitochondrial impairment in heart failure(130) and ischemic-induced reductions in skeletal muscle energetics in patients with PAD.(121,127,131–136) PCr re-synthesis

following ischemia/exercise is only possible through the CK system and requires adenosine triphosphate, produced predominantly by mitochondrial oxidative phosphorylation. Hence, PCr/Cr CEST detection of PCr re-synthesis can be an approach for detecting and quantifying defects in mitochondrial oxidative phosphorylation as demonstrated on the patients with Friedreich's ataxia (137).

Clinical Translation of PCr, Cr and ArgCEST—Clinical translation of CEST methods on human scanners is challenging mainly due to the relatively low signal (<2%) that is susceptible to interference by many artifacts. CrCEST has already been demonstrated on both 3T and 7T clinical MRI scanners,(54,122) while PCrCEST has been demonstrated on 3T MRI scanners (51). Human studies on PCr/Cr CEST were still limited to the muscle due to the requirement of high PCr and Cr concentration for adequate sensitivity. The first two major factors to consider for the clinical translation is B_0 and B_1 inhomogeneity. B_0 inhomogeneity is about ±0.5 ppm for the human brain (37,88,96) and ±0.4 ppm for the leg at 3T (51,54). B_0 compensation can be achieved by acquiring a wider range of the Z-spectrum and an extra B_0 map. The standard deviation of the B_1 maps is about 10% for the human brain (37,88,96) and 20% for the leg at 3T (51,54). The correction of B_1 inhomogeneity can be achieved by B_1 insensitive saturation schemes, such as pulsed saturation with long mixing times (37), or by acquiring multiple Z-spectra with different B_1 values (138). In most cases, both B_0 and B_1 compensation will extend the total scan time significantly. Patient movement is another issue when performing human studies, particularly during plantar flexion exercise. This can be solved by image post-processing such as image registration or using motion insensitive MRI readout schemes such as steady-state radial CEST (starCEST). (37)

Specificity is also a major issue in clinical translation. PCr shows one well defined peak at 3T and can be extended and quantified with the PLOF or ANNCEST methods. Although CrCEST was used in human CK measurements,(54,80) it is difficult to derive concentrations from Cr CEST due to the broad and indiscernible CEST peak induced by the fast exchange rate of Cr guanidinium protons in tissue (950 ± 100 s^{-1}). (46)There are limited options for quantifying CrCEST in human studies. Up to now, it was mainly achieved with MTasym, which has a high temporal resolution but is susceptible to interference by T_1/T_2 changes (54). Therefore, there is still need for further development before the standardization of CrCEST acquisition and quantification for clinical application. ArgCEST is clearly visible in the human brain Z-spectrum on 9.4T MRI (38,138,139), hence, can be extracted with the PLOF method. On the contrary, the ArgCEST peak is too low to be visible at 3T (37,88,96). Although, the CEST maps at 2 ppm has been reported (58), specific ArgCEST maps of human brain have yet to be achieved at 3T and high MRI fields.

Conclusion

In recognition of the value of imaging Arg, Cr and PCr through CEST, much work has been done to understanding and validating the signal sources behind what is observed when attempting to image these molecular targets. In this review, we have seen initial works demonstrating the potential of monitoring energy metabolism through imaging the Cr/PCr metabolite components of the creatine phosphate pathway as well as other possibilities such

as protein imaging using ArgCEST. The enhanced pH mapping with ArgCEST, CrCEST and PCrCEST are also possible due in part to their ubiquitous presence in various tissues. Although the potential contamination from resonances with close or redundant frequencies may still raise questions of precise quantification, both advances in separating out non-specific signals as well as redefining goals to meet specific diagnostic needs, such as focusing on dynamic changes over definitive quantification, bring workable solutions closer to realization. Moving forward, the future of CEST imaging of Arg, Cr and PCr will depend on the advancement of technical know-how in obtaining increasingly specific signals as well as the identification of potential clinical needs and understanding the key parameters to meet them.

Supplementary Material

Refer to Web version on PubMed Central for supplementary material.

Acknowledgments

Grant support from NIH: P41EB031771, R01HL149742, R01NS100703

Abbreviations used:

CEST	chemical exchange saturation transfer
MTC	magnetization transfer contrast
PLOF	Polynomial and Lorentzian Line-shape Fitting
Cr	creatine
PCr	Phosphocreatine
NOE	nuclear Overhauser enhancement
ppm	parts per million
RF	radiofrequenc
DS	direct water saturation
FOV	field of view
BSA	bovine serum albumin
ROI	region of interest
WT	wild type mouse
PBS	phosphate buffered saline
Glu	glutamate
Guan	Guanidinium

GAMT	guanidinoacetate methyltransferase
ANN	artificial neural networks
CK	creatine kinase reaction

References:

1. Ward K, Aletras A, Balaban RS. A new class of contrast agents for MRI based on proton chemical exchange dependent saturation transfer (CEST). J Magn Reson 2000;143(1):79–87. [PubMed: 10698648]
2. Van Zijl PC, Yadav NN. Chemical exchange saturation transfer (CEST): what is in a name and what isn't? Magn Reson Med 2011;65(4):927–948. [PubMed: 21337419]
3. Zhou J, van Zijl PCM. Chemical exchange saturation transfer imaging and spectroscopy. Progress in Nuclear Magnetic Resonance Spectroscopy 2006;48(2–3):109–136.
4. Woessner DE, Zhang S, Merritt ME, Sherry AD. Numerical solution of the Bloch equations provides insights into the optimum design of PARACEST agents for MRI. Magn Reson Med 2005;53(4):790–799. [PubMed: 15799055]
5. Liu G, Song X, Chan KW, McMahon MT. Nuts and bolts of chemical exchange saturation transfer MRI. NMR Biomed 2013;26(7):810–828. [PubMed: 23303716]
6. Aime S, Castelli DD, Crich SG, Gianolio E, Terreno E. Pushing the sensitivity envelope of lanthanide-based magnetic resonance imaging (MRI) contrast agents for molecular imaging applications. Accounts Chem Res 2009;42(7):822–831.
7. van Zijl PC, Lam WW, Xu J, Knutsson L, Stanisz GJ. Magnetization transfer contrast and chemical exchange saturation transfer MRI. Features and analysis of the field-dependent saturation spectrum. NeuroImage 2018;168:222–241. [PubMed: 28435103]
8. Jones KM, Pollard AC, Pagel MD. Clinical applications of chemical exchange saturation transfer (CEST) MRI. J Magn Reson Imaging 2018;47(1):11–27. [PubMed: 28792646]
9. Wolff S, Balaban R. NMR imaging of labile proton exchange. J Magn Reson 1990;86:164–169.
10. Zhou J, Payen JF, Wilson DA, Traystman RJ, van Zijl PC. Using the amide proton signals of intracellular proteins and peptides to detect pH effects in MRI. Nat Med 2003;9(8):1085–1090. [PubMed: 12872167]
11. Zhou J, Lal B, Wilson DA, Laterra J, van Zijl PCM. Amide proton transfer (APT) contrast for imaging of brain tumors. Magn Reson Med 2003;50(6):1120–1126. [PubMed: 14648559]
12. Sun PZ, Zhou J, Sun W, Huang J, van Zijl PCM. Detection of the ischemic penumbra using pH-weighted MRI. J Cereb Blood Flow Metab 2006;27(6):1129–1136. [PubMed: 17133226]
13. Jia G, Abaza R, Williams JD, Zynger DL, Zhou J, Shah ZK, Patel M, Sammet S, Wei L, Bahnson RR, Knopp MV. Amide proton transfer MR imaging of prostate cancer: a preliminary study. J Magn Reson Imaging 2011;33(3):647–654. [PubMed: 21563248]
14. Jin T, Wang P, Zong X, Kim S-G. Magnetic resonance imaging of the Amine–Proton EXchange (APEX) dependent contrast. NeuroImage 2012;59(2):1218–1227. [PubMed: 21871570]
15. Li C, Peng S, Wang R, Chen H, Su W, Zhao X, Zhou J, Chen M. Chemical exchange saturation transfer MR imaging of Parkinson's disease at 3 Tesla. European radiology 2014;24(10):2631–2639. [PubMed: 25038850]
16. Desmond KL, Moosvi F, Stanisz GJ. Mapping of amide, amine, and aliphatic peaks in the CEST spectra of murine xenografts at 7 T. Magn Reson Med 2014;71(5):1841–1853. [PubMed: 23801344]
17. Cai K, Singh A, Poptani H, Li W, Yang S, Lu Y, Hariharan H, Zhou XJ, Reddy R. CEST signal at 2ppm (CEST@2ppm) from Z-spectral fitting correlates with creatine distribution in brain tumor. NMR Biomed 2015;28(1):1–8. [PubMed: 25295758]
18. Chen LQ, Pagel MD. Evaluating pH in the Extracellular Tumor Microenvironment Using CEST MRI and Other Imaging Methods. Adv Radiol 2015;2015(2015):pii: 206405. [PubMed: 27761517]

19. Donahue MJ, Donahue PC, Rane S, Thompson CR, Strother MK, Scott AO, Smith SA. Assessment of lymphatic impairment and interstitial protein accumulation in patients with breast cancer treatment-related lymphedema using CEST MRI. Magn Reson Med 2016;75(1):345–355. [PubMed: 25752499]
20. Zhou J, Heo HY, Knutsson L, van Zijl PCM, Jiang S. APT-weighted MRI: Techniques, current neuro applications, and challenging issues. J Magn Reson Imaging 2019;50(2):347–364. [PubMed: 30663162]
21. Chen L, Wei Z, Chan KWY, Cai S, Liu G, Lu H, Wong PC, van Zijl PCM, Li T, Xu J. Protein aggregation linked to Alzheimer's disease revealed by saturation transfer MRI. Neuroimage 2018;188:380–390. [PubMed: 30553917]
22. van Zijl PC, Jones CK, Ren J, Malloy CR, Sherry AD. MRI detection of glycogen in vivo by using chemical exchange saturation transfer imaging (glycoCEST). Proc Natl Acad Sci U S A 2007;104(11):4359–4364. [PubMed: 17360529]
23. Ling W, Regatte RR, Navon G, Jerschow A. Assessment of glycosaminoglycan concentration in vivo by chemical exchange-dependent saturation transfer (gagCEST). Proc Natl Acad Sci USA 2008;105(7):2266–2270. [PubMed: 18268341]
24. Cai K, Haris M, Singh A, Kogan F, Greenberg JH, Hariharan H, Detre JA, Reddy R. Magnetic resonance imaging of glutamate. Nat Med 2012;18(2):302–306. [PubMed: 22270722]
25. Davis KA, Nanga RP, Das S, Chen SH, Hadar PN, Pollard JR, Lucas TH, Shinohara RT, Litt B, Hariharan H, Elliott MA, Detre JA, Reddy R. Glutamate imaging (GluCEST) lateralizes epileptic foci in nonlesional temporal lobe epilepsy. Sci Transl Med 2015;7(309):309ra161.
26. DeBrosse C, Nanga RP, Bagga P, Nath K, Haris M, Marincola F, Schnall MD, Hariharan H, Reddy R. Lactate Chemical Exchange Saturation Transfer (LATEST) Imaging in vivo A Biomarker for LDH Activity. Sci Rep 2016;6:19517. [PubMed: 26794265]
27. Zhou J, Tryggestad E, Wen Z, Lal B, Zhou T, Grossman R, Wang S, Yan K, Fu DX, Ford E, Tyler B, Blakeley J, Laterra J, van Zijl PC. Differentiation between glioma and radiation necrosis using molecular magnetic resonance imaging of endogenous proteins and peptides. Nat Med 2011;17(1):130–134. [PubMed: 21170048]
28. Zong X, Wang P, Kim SG, Jin T. Sensitivity and source of amine-proton exchange and amide-proton transfer magnetic resonance imaging in cerebral ischemia. Magn Reson Med 2014;71(1):118–132. [PubMed: 23401310]
29. Chen L, Cao S, Koehler RC, van Zijl PCM, Xu J. High-sensitivity CEST mapping using a spatiotemporal correlation-enhanced method. Magn Reson Med 2020;84(6):3342–3350. [PubMed: 32597519]
30. Harris RJ, Cloughesy TF, Liau LM, Nghiemphu PL, Lai A, Pope WB, Ellingson BM. Simulation, phantom validation, and clinical evaluation of fast pH-weighted molecular imaging using amine chemical exchange saturation transfer echo planar imaging (CEST-EPI) in glioma at 3 T. NMR Biomed 2016;29(11):1563–1576. [PubMed: 27717216]
31. Cui J, Zhang X-Y, Xie J, Gochberg FD, Zu Z. Towards the molecular origin of glutamate CEST (GluCEST) imaging in rat brain. Magn Reson Med 2020;83(4):1405–1417. [PubMed: 31691367]
32. Wermter FC, Bock C, Dreher W. Characterization of amine proton exchange for analyzing the specificity and intensity of the CEST effect: from humans to fish. NMR Biomed 2021:e4622. [PubMed: 34605080]
33. Jin T, Wang P, Hitchens TK, Kim SG. Enhancing sensitivity of pH-weighted MRI with combination of amide and guanidyl CEST. Neuroimage 2017;157:341–350. [PubMed: 28602944]
34. Zhang XY, Xie J, Wang F, Lin EC, Xu J, Gochberg DF, Gore JC, Zu Z. Assignment of the molecular origins of CEST signals at 2 ppm in rat brain. Magn Reson Med 2017;78(3):881–887. [PubMed: 28653349]
35. Chen L, Zeng H, Xu X, Yadav NN, Cai S, Puts NA, Barker PB, Li T, Weiss RG, van Zijl PCM, Xu J. Investigation of the contribution of total creatine to the CEST Z-spectrum of brain using a knockout mouse model. NMR Biomed 2017;30(12):e3834.
36. Zhou IY, Lu D, Ji Y, Wu L, Wang E, Cheung JS, Zhang XA, Sun PZ. Determination of multipool contributions to endogenous amide proton transfer effects in global ischemia with high spectral

resolution in vivo chemical exchange saturation transfer MRI. Magn Reson Med 2019;81(1):645–652. [PubMed: 30058148]

37. Sui R, Chen L, Li Y, Huang J, Chan KWY, Xu X, Zijl PCMv, Xu J Whole-brain amide CEST imaging at 3T with a steady-state radial MRI acquisition. Magn Reson Med 2021;86(2):893–906. [PubMed: 33772859]
38. Zaiss M, Windschuh J, Goerke S, Paech D, Meissner JE, Burth S, Kickingereder P, Wick W, Bendszus M, Schlemmer HP, Ladd ME, Bachert P, Radbruch A. Downfield-NOE-suppressed amide-CEST-MRI at 7 Tesla provides a unique contrast in human glioblastoma. Magn Reson Med 2017;77(1):196–208. [PubMed: 26845067]
39. Chen L, Xu X, Zeng H, Chan K, Yadav NN, Cai S, Schunke KJ, Faraday N, van Zijl PCM, Xu J. Separating Fast and Slow Exchange Transfer and Magnetization Transfer Using Off-resonance Variable Delay Multiple Pulse (VDMP) MRI. Magn Reson Med 2018;80(4):1568–1576. [PubMed: 29405374]
40. Haris M, Singh A, Cai K, Nath K, Crescenzi R, Kogan F, Hariharan H, Reddy R. MICEST: a potential tool for non-invasive detection of molecular changes in Alzheimer's disease. J Neurosci Methods 2013;212(1):87–93. [PubMed: 23041110]
41. Jones CK, Huang A, Xu J, Edden RA, Schar M, Hua J, Oskolkov N, Zaca D, Zhou J, McMahon MT, Pillai JJ, van Zijl PC. Nuclear Overhauser enhancement (NOE) imaging in the human brain at 7T. NeuroImage 2013;77C:114–124.
42. Xu J, Yadav NN, Bar-Shir A, Jones CK, Chan KW, Zhang J, Walczak P, McMahon MT, van Zijl PC. Variable delay multi-pulse train for fast chemical exchange saturation transfer and relayed-nuclear overhauser enhancement MRI. Magn Reson Med 2014;71(5):1798–1812. [PubMed: 23813483]
43. Xu X, Yadav NN, Zeng H, Jones CK, Zhou J, van Zijl PC, Xu J. Magnetization transfer contrast–suppressed imaging of amide proton transfer and relayed nuclear overhauser enhancement chemical exchange saturation transfer effects in the human brain at 7T. Magn Reson Med 2016;75(1):88–96. [PubMed: 26445350]
44. Jones CK, Huang A, Xu J, Edden RA, Schär M, Hua J, Oskolkov N, Zacà D, Zhou J, McMahon MT. Nuclear Overhauser enhancement (NOE) imaging in the human brain at 7 T. NeuroImage 2013;77:114–124. [PubMed: 23567889]
45. Jin T, Wang P, Zong X, Kim S-G. MR imaging of the amide-proton transfer effect and the pH-insensitive nuclear overhauser effect at 9.4 T. Magn Reson Med 2013;69(3):760–770. [PubMed: 22577042]
46. Haris M, Nanga RP, Singh A, Cai K, Kogan F, Hariharan H, Reddy R. Exchange rates of creatine kinase metabolites: feasibility of imaging creatine by chemical exchange saturation transfer MRI. NMR Biomed 2012;25(11):1305–1309. [PubMed: 22431193]
47. Sun PZ, Farrar CT, Sorensen AG. Correction for artifacts induced by B(0) and B(1) field inhomogeneities in pH-sensitive chemical exchange saturation transfer (CEST) imaging. Magn Reson Med 2007;58(6):1207–1215. [PubMed: 17969015]
48. Sun PZ, Benner T, Kumar A, Sorensen AG. Investigation of optimizing and translating pH-sensitive pulsed-chemical exchange saturation transfer (CEST) imaging to a 3T clinical scanner. Magn Reson Med 2008;60(4):834–841. [PubMed: 18816867]
49. Liu P, Jing Y, Collie ND, Dean B, Bilkey DK, Zhang H. Altered brain arginine metabolism in schizophrenia. Transl Psychiatry 2016;6:e871. [PubMed: 27529679]
50. Goerke S, Zaiss M, Bachert P. Characterization of creatine guanidinium proton exchange by water-exchange (WEX) spectroscopy for absolute-pH CEST imaging in vitro. NMR Biomed 2014;27(5):507–518. [PubMed: 24535718]
51. Chen L, Schar M, Chan KWY, Huang J, Wei Z, Lu H, Qin Q, Weiss RG, van Zijl PCM, Xu J. In vivo imaging of phosphocreatine with artificial neural networks. Nat Commun 2020;11(1):1072. [PubMed: 32102999]
52. Chen L, Barker PB, Weiss RG, van Zijl PCM, Xu J. Creatine and phosphocreatine mapping of mouse skeletal muscle by a polynomial and Lorentzian line-shape fitting CEST method. Magn Reson Med 2019;81(1):69–78. [PubMed: 30246265]

53. Kogan F, Haris M, Singh A, Cai K, Debrosse C, Nanga RP, Hariharan H, Reddy R. Method for high-resolution imaging of creatine in vivo using chemical exchange saturation transfer. Magn Reson Med 2014;71(1):164–172. [PubMed: 23412909]
54. Kogan F, Haris M, Debrosse C, Singh A, Nanga RP, Cai K, Hariharan H, Reddy R. In vivo chemical exchange saturation transfer imaging of creatine (CrCEST) in skeletal muscle at 3T. J Magn Reson Imaging 2014;40(3):596–602. [PubMed: 24925857]
55. McMahon MT, Gilad AA, DeLiso MA, Berman SM, Bulte JW, van Zijl PC. New "multicolor" polypeptide diamagnetic chemical exchange saturation transfer (DIACEST) contrast agents for MRI. Magn Reson Med 2008;60(4):803–812. [PubMed: 18816830]
56. Cui J, Afzal A, Zu Z. Comparative evaluation of polynomial and Lorentzian lineshape-fitted amine CEST imaging in acute ischemic stroke. Magn Reson Med 2021:10.1002/mrm.29030.
57. Chen L, Xu J. The sensitivity of amide, amine, creatine and guanidinium CEST in detecting pH at high MRI field. 2021; virtual. Proceedings of the 20th Annual Meeting of ISMRM. p 1195.
58. Zaiss M, Deshmane A, Schuppert M, Herz K, Glang F, Ehses P, Lindig T, Bender B, Ernemann U, Scheffler K. DeepCEST: 9.4 T Chemical exchange saturation transfer MRI contrast predicted from 3 T data - a proof of concept study. Magn Reson Med 2019;81(6):3901–3914. [PubMed: 30803000]
59. Jin T, Kim SG. Approximated analytical characterization of the steady-state chemical exchange saturation transfer (CEST) signals. Magn Reson Med 2019;82(5):1876–1889. [PubMed: 31237027]
60. Zong X, Wang P, Kim SG, Jin T. Sensitivity and source of amine-proton exchange and amide-proton transfer magnetic resonance imaging in cerebral ischemia. Magn Reson Med 2014;71(1):118–132. [PubMed: 23401310]
61. Jin T, Kim SG. Role of chemical exchange on the relayed nuclear Overhauser enhancement signal in saturation transfer MRI. Magn Reson Med 2021:10.1002/mrm.28961.
62. Renema WK, Schmidt A, van Asten JJ, Oerlemans F, Ullrich K, Wieringa B, Isbrandt D, Heerschap A. MR spectroscopy of muscle and brain in guanidinoacetate methyltransferase (GAMT)-deficient mice: validation of an animal model to study creatine deficiency. Magn Reson Med 2003;50(5):936–943. [PubMed: 14587004]
63. Schmidt A, Marescau B, Boehm EA, Renema WK, Peco R, Das A, Steinfeld R, Chan S, Wallis J, Davidoff M, Ullrich K, Waldschutz R, Heerschap A, De Deyn PP, Neubauer S, Isbrandt D. Severely altered guanidino compound levels, disturbed body weight homeostasis and impaired fertility in a mouse model of guanidinoacetate N-methyltransferase (GAMT) deficiency. Hum Mol Genet 2004;13(9):905–921. [PubMed: 15028668]
64. Kan HE, Meeuwissen E, van Asten JJ, Veltien A, Isbrandt D, Heerschap A. Creatine uptake in brain and skeletal muscle of mice lacking guanidinoacetate methyltransferase assessed by magnetic resonance spectroscopy. J Appl Physiol 2007;102(6):2121–2127. [PubMed: 17347380]
65. Comeaux MS, Wang J, Wang G, Kleppe S, Zhang VW, Schmitt ES, Craigen WJ, Renaud D, Sun Q, Wong LJ. Biochemical, molecular, and clinical diagnoses of patients with cerebral creatine deficiency syndromes. Mol Genet Metab 2013;109(3):260–268. [PubMed: 23660394]
66. Chen L, Wei Z, Cai S, Li Y, Liu G, Lu H, Weiss RG, van Zijl PCM, Xu J. High-resolution creatine mapping of mouse brain at 11.7 T using non-steady-state chemical exchange saturation transfer. NMR Biomed 2019;32(11):e4168. [PubMed: 31461196]
67. Renema WKJ, Schmidt A, van Asten JJ, Oerlemans F, Ullrich K, Wieringa B, Isbrandt D, Heerschap A. MR spectroscopy of muscle and brain in guanidinoacetate methyltransferase (GAMT)-deficient mice: validation of an animal model to study creatine deficiency. Magn Reson Med 2003;50(5):936–943. [PubMed: 14587004]
68. t Zandt Hi, Groof Ad, Renema W, Oerlemans F, Klomp D, Wieringa B, Heerschap A. Presence of (phospho) creatine in developing and adult skeletal muscle of mice without mitochondrial and cytosolic muscle creatine kinase isoforms. The Journal of physiology 2003;548(3):847–858. [PubMed: 12640020]
69. Chung JJ, Jin T, Lee JH, Kim SG. Chemical exchange saturation transfer imaging of phosphocreatine in the muscle. Magn Reson Med 2019;81(6):3476–3487. [PubMed: 30687942]

70. Zu Z, Lin EC, Louie EA, Jiang X, Lankford CL, Damon B, Does MD, Gore JC, Gochberg DF. Chemical exchange rotation transfer imaging of phosphocreatine in muscle. NMR Biomed 2021;34(2):e4437. [PubMed: 33283945]
71. Chen YW, Liu HQ, Wu Q, Huang YH, Tung YY, Lin MH, Lin CH, Chen TC, Lin EC, Hwang DW. pH Mapping of Skeletal Muscle by Chemical Exchange Saturation Transfer (CEST) Imaging. Cells 2020;9(12).
72. Bertram HC, Donstrup S, Karlsson AH, Andersen HJ, Stodkilde-Jorgensen H. Post mortem energy metabolism and pH development in porcine M. longissimus dorsi as affected by two different cooling regimes. A (31)P-NMR spectroscopic study. Magn Reson Imaging 2001;19(7):993–1000. [PubMed: 11595371]
73. in 't Zandt HJ, de Groof AJ, Renema WK, Oerlemans FT, Klomp DW, Wieringa B, Heerschap A. Presence of (phospho)creatine in developing and adult skeletal muscle of mice without mitochondrial and cytosolic muscle creatine kinase isoforms. J Physiol 2003;548(Pt 3):847–858. [PubMed: 12640020]
74. Zhou Y, van Zijl PCM, Xu J, Yadav NN. Mechanism and quantitative assessment of saturation transfer for water-based detection of the aliphatic protons in carbohydrate polymers. Magn Reson Med 2021;85(3):1643–1654. [PubMed: 32970889]
75. Chen Lin, van Zijl Peter C.M., Wei Zhiliang, Hanzhang Lu, Duan Wenzhen, Wong Philip C., Li Tong, Xu J. Early detection of Alzheimer's disease using creatine chemical exchange saturation transfer magnetic resonance imaging. NeuroImage 2021;236:118071. [PubMed: 33878375]
76. Zhou J, Blakeley JO, Hua J, Kim M, Laterra J, Pomper MG, van Zijl PC. Practical data acquisition method for human brain tumor amide proton transfer (APT) imaging. Magn Reson Med 2008;60(4):842–849. [PubMed: 18816868]
77. Heo HY, Zhang Y, Burton TM, Jiang S, Zhao Y, van Zijl PCM, Leigh R, Zhou J. Improving the detection sensitivity of pH-weighted amide proton transfer MRI in acute stroke patients using extrapolated semisolid magnetization transfer reference signals. Magn Reson Med 2017;78(3):871–880. [PubMed: 28639301]
78. Huang J, Han X, Chen L, Xu X, Xu J, Chan KWY. Relayed nuclear Overhauser enhancement imaging with magnetization transfer contrast suppression at 3 T. Magn Reson Med 2021;85(1):254–267. [PubMed: 32738080]
79. Jin T, Kim SG. Advantages of chemical exchange-sensitive spin-lock (CESL) over chemical exchange saturation transfer (CEST) for hydroxyl- and amine-water proton exchange studies. NMR Biomed 2014;27(11):1313–1324. [PubMed: 25199631]
80. Haris M, Singh A, Cai K, Kogan F, McGarvey J, Debrosse C, Zsido GA, Witschey WR, Koomalsingh K, Pilla JJ, Chirinos JA, Ferrari VA, Gorman JH, Hariharan H, Gorman RC, Reddy R. A technique for in vivo mapping of myocardial creatine kinase metabolism. Nat Med 2014;20(2):209–214. [PubMed: 24412924]
81. Hua J, Jones CK, Blakeley J, Smith SA, van Zijl PC, Zhou J. Quantitative description of the asymmetry in magnetization transfer effects around the water resonance in the human brain. Magn Reson Med 2007;58(4):786–793. [PubMed: 17899597]
82. Xu J, Yadav NN, Bar-Shir A, Jones CK, Chan KW, Zhang J, Walczak P, McMahon MT, Van Zijl PC. Variable delay multi-pulse train for fast chemical exchange saturation transfer and relayed-nuclear overhauser enhancement MRI. Magn Reson Med 2014;71(5):1798–1812. [PubMed: 23813483]
83. Zhou J, Hong X, Zhao X, Gao JH, Yuan J. APT-weighted and NOE-weighted image contrasts in glioma with different RF saturation powers based on magnetization transfer ratio asymmetry analyses. Magn Reson Med 2013;70(2):320–327. [PubMed: 23661598]
84. Heo HY, Zhang Y, Lee DH, Hong X, Zhou J. Quantitative assessment of amide proton transfer (APT) and nuclear Overhauser enhancement (NOE) imaging with extrapolated semi-solid magnetization transfer reference (EMR) signals: application to a rat glioma model at 4.7 Tesla. Magn Reson Med 2016;75(1):137–149. [PubMed: 25753614]
85. Heo HY, Zhang Y, Burton TM, Jiang S, Zhao Y, van Zijl PC, Leigh R, Zhou J. Improving the detection sensitivity of p H-weighted amide proton transfer MRI in acute stroke patients using extrapolated semisolid magnetization transfer reference signals. Magn Reson Med 2017;78(3):871–880. [PubMed: 28639301]

86. Zaiss M, Windschuh J, Goerke S, Paech D, Meissner JE, Burth S, Kickingereder P, Wick W, Bendszus M, Schlemmer HP, Ladd ME, Bachert P, Radbruch A. Downfield-NOE-suppressed amide-CEST-MRI at 7 Tesla provides a unique contrast in human glioblastoma. Magn Reson Med 2016.
87. Zhou IY, Wang E, Cheung JS, Zhang X, Fulci G, Sun PZ. Quantitative chemical exchange saturation transfer (CEST) MRI of glioma using Image Downsampling Expedited Adaptive Least-squares (IDEAL) fitting. Scientific Reports 2017;7(1):84. [PubMed: 28273886]
88. Mueller S, Stirnberg R, Akbey S, Ehses P, Scheffler K, Stocker T, Zaiss M. Whole brain snapshot CEST at 3T using 3D-EPI: Aiming for speed, volume, and homogeneity. Magn Reson Med 2020;84(5):2469–2483. [PubMed: 32385888]
89. Trott O, Palmer AG. R 1ρ relaxation outside of the fast-exchange limit. J Magn Reson 2002;154(1):157–160. [PubMed: 11820837]
90. Jin T, Autio J, Obata T, Kim SG. Spin-locking versus chemical exchange saturation transfer MRI for investigating chemical exchange process between water and labile metabolite protons. Magn Reson Med 2011;65(5):1448–1460. [PubMed: 21500270]
91. Zaiss M, Bachert P. Chemical exchange saturation transfer (CEST) and MR Z - spectroscopy in vivo : a review of theoretical approaches and methods. Phys Med Biol 2013;58(22):R221. [PubMed: 24201125]
92. Zaiss M, Bachert P. Exchange-dependent relaxation in the rotating frame for slow and intermediate exchange -- modeling off-resonant spin-lock and chemical exchange saturation transfer. NMR Biomed 2013;26(5):507–518. [PubMed: 23281186]
93. Zhu B, Liu JZ, Cauley SF, Rosen BR, Rosen MS. Image reconstruction by domain-transform manifold learning. Nature 2018;555(7697):487–492. [PubMed: 29565357]
94. Qi D, Hao C, Lequan Y, Lei Z, Jing Q, Defeng W, Mok VC, Lin S, Pheng-Ann H. Automatic Detection of Cerebral Microbleeds From MR Images via 3D Convolutional Neural Networks. IEEE Trans Med Imaging 2016;35(5):1182–1195. [PubMed: 26886975]
95. Pereira S, Pinto A, Alves V, Silva CA. Brain Tumor Segmentation Using Convolutional Neural Networks in MRI Images. IEEE Trans Med Imaging 2016;35(5):1240–1251. [PubMed: 26960222]
96. Glang F, Deshmane A, Prokudin S, Martin F, Herz K, Lindig T, Bender B, Scheffler K, Zaiss M. DeepCEST 3T: Robust MRI parameter determination and uncertainty quantification with neural networks-application to CEST imaging of the human brain at 3T. Magn Reson Med 2020;84(1):450–466. [PubMed: 31821616]
97. Cai K, Tain RW, Zhou XJ, Damen FC, Scotti AM, Hariharan H, Poptani H, Reddy R. Creatine CEST MRI for Differentiating Gliomas with Different Degrees of Aggressiveness. Mol Imaging Biol 2017;19(2):225–232. [PubMed: 27541025]
98. Jiang S, Eberhart CG, Zhang Y, Heo HY, Wen Z, Blair L, Qin H, Lim M, Quinones-Hinojosa A, Weingart JD, Barker PB, Pomper MG, Laterra J, van Zijl PCM, Blakeley JO, Zhou J. Amide proton transfer-weighted magnetic resonance image-guided stereotactic biopsy in patients with newly diagnosed gliomas. Eur J Cancer 2017;83:9–18. [PubMed: 28704644]
99. Faubert B, Li KY, Cai L, Hensley CT, Kim J, Zacharias LG, Yang C, Do QN, Doucette S, Burguete D, Li H, Huet G, Yuan Q, Wigal T, Butt Y, Ni M, Torrealba J, Oliver D, Lenkinski RE, Malloy CR, Wachsmann JW, Young JD, Kernstine K, DeBerardinis RJ. Lactate Metabolism in Human Lung Tumors. Cell 2017;171(2):358–371 e359. [PubMed: 28985563]
100. Kim H, Krishnamurthy LC, Sun PZ. Brain pH Imaging and its Applications. Neuroscience 2021;S0306–4522(21):00033.
101. Rahman MA, Kumar P, Park DS, Shim YB. Electrochemical Sensors Based on Organic Conjugated Polymers. Sensors (Basel) 2008;8(1):118–141. [PubMed: 27879698]
102. Shi XM, Mei LP, Zhang N, Zhao WW, Xu JJ, Chen HY. A Polymer Dots-Based Photoelectrochemical pH Sensor: Simplicity, High Sensitivity, and Broad-Range pH Measurement. Anal Chem 2018;90(14):8300–8303. [PubMed: 29956537]
103. Wencel D, Abel T, McDonagh C. Optical chemical pH sensors. Anal Chem 2014;86(1):15–29. [PubMed: 24180284]

104. Jensen KE, Thomsen C, Henriksen O. n vivo measurement of intracellular pH in human brain during different tensions of carbon dioxide in arterial blood. A 31P-NMR study. Acta Ph-ysiol Scand 1988;134:295–292g298.
105. Nishimura M, Johnson DC, Hitzig BM, Okunieff P, Kazemi H. Effects of hypercapnia on brain pHi and phosphate metabolite regulation by 31P-NMR. J Appl Physiol (1985) 1989;66(5):2181–2188. [PubMed: 2501277]
106. Petroff OA, Prichard JW, Behar KL, Alger JR, den Hollander JA, Shulman RG. Cerebral intracellular pH by 31P nuclear magnetic resonance spectroscopy. Neurology 1985;35(6):781–788. [PubMed: 4000479]
107. Gil MS, Cruz F, Cerdán S, Ballesteros P. Imidazol-1-ylalkanoate esters and their corresponding acids. A novel series of extrinsic 1H NMR probes for intracellular pH. Bioorganic & Medicinal Chemistry Letters 1992;2(12):1717–1722.
108. Lyros E, Ragoschke-Schumm A, Kostopoulos P, Sehr A, Backens M, Kalampokini S, Decker Y, Lesmeister M, Liu Y, Reith W, Fassbender K. Normal brain aging and Alzheimer's disease are associated with lower cerebral pH: an in vivo histidine (1)H-MR spectroscopy study. Neurobiol Aging 2020;87:60–69. [PubMed: 31902521]
109. Vermathen P, Capizzano AA, Maudsley AA. Administration and (1)H MRS detection of histidine in human brain: application to in vivo pH measurement. Magn Reson Med 2000;43(5):665–675. [PubMed: 10800031]
110. Coman D, Peters DC, Walsh JJ, Savic LJ, Huber S, Sinusas AJ, Lin M, Chapiro J, Constable RT, Rothman DL, Duncan JS, Hyder F. Extracellular pH mapping of liver cancer on a clinical 3T MRI scanner. Magn Reson Med 2020;83(5):1553–1564. [PubMed: 31691371]
111. Foo LS, Larkin JR, Sutherland BA, Ray KJ, Yap WS, Hum YC, Lai KW, Manan HA, Sibson NR, Tee YK. Study of common quantification methods of amide proton transfer magnetic resonance imaging for ischemic stroke detection. Magn Reson Med 2021;85(4):2188–2200. [PubMed: 33107119]
112. Sun PZ, Xiao G, Zhou IY, Guo Y, Wu R. A method for accurate pH mapping with chemical exchange saturation transfer (CEST) MRI. Contrast Media Mol Imaging 2016;11(3):195–202. [PubMed: 26689424]
113. Leigh R, Knutsson L, Zhou J, van Zijl PC. Imaging the physiological evolution of the ischemic penumbra in acute ischemic stroke. J Cereb Blood Flow Metab 2018;38(9):1500–1516. [PubMed: 28345479]
114. Martoft L, Stodkilde-Jorgensen H, Forslid A, Pedersen HD, Jorgensen PF. CO2 induced acute respiratory acidosis and brain tissue intracellular pH: a P-31 NMR study in swine. Laboratory Animals 2003;37(3):241–248. [PubMed: 12869287]
115. Wyss M, Kaddurah-daouk R. Creatine and Creatinine Metabolism. Physiol Rev 2000;80:1107. [PubMed: 10893433]
116. Andres RH, Ducray AD, Schlattner U, Wallimann T, Widmer HR. Functions and effects of creatine in the central nervous system. Brain Res Bull 2008;76(4):329–343. [PubMed: 18502307]
117. Schlattner U, Tokarska-Schlattner M, Wallimann T. Mitochondrial creatine kinase in human health and disease. Biochim Biophys Acta 2006;1762(2):164–180. [PubMed: 16236486]
118. Boesch C Musculoskeletal spectroscopy. J Magn Reson Imaging 2007;25(2):321–338. [PubMed: 17260389]
119. Bottomley PA, Lee Y, Weiss RG. Total creatine in muscle: imaging and quantification with proton MR spectroscopy. Radiology 1997;204(2):403–410. [PubMed: 9240527]
120. Prompers JJ, Jeneson JA, Drost MR, Oomens CC, Strijkers GJ, Nicolay K. Dynamic MRS and MRI of skeletal muscle function and biomechanics. NMR Biomed 2006;19(7):927–953. [PubMed: 17075956]
121. Kemp GJ, Meyerspeer M, Moser E. Absolute quantification of phosphorus metabolite concentrations in human muscle in vivo by 31P MRS: a quantitative review. NMR Biomed 2007;20(6):555–565. [PubMed: 17628042]
122. Kumar D, Nanga RPR, Thakuri D, Wilson N, Cember A, Martin ML, Zhu D, Shinohara RT, Qin Q, Hariharan H, Reddy R. Recovery kinetics of creatine in mild plantar flexion exercise using 3D creatine CEST imaging at 7 Tesla. Magn Reson Med 2021;85(2):802–817. [PubMed: 32820572]

123. Schmid AI, Meyerspeer M, Robinson SD, Goluch S, Wolzt M, Fiedler GB, Bogner W, Laistler E, Krssak M, Moser E, Trattnig S, Valkovic L. Dynamic PCr and pH imaging of human calf muscles during exercise and recovery using (31) P gradient-Echo MRI at 7 Tesla. Magn Reson Med 2016;75(6):2324–2331. [PubMed: 26115021]

124. Fiedler GB, Meyerspeer M, Schmid AI, Goluch S, Schewzow K, Laistler E, Mirzahosseini A, Niess F, Unger E, Wolzt M, Moser E. Localized semi-LASER dynamic (31)P magnetic resonance spectroscopy of the soleus during and following exercise at 7 T. Magma 2015;28(5):493–501. [PubMed: 25894813]

125. Valkovic L, Chmelik M, Meyerspeer M, Gagoski B, Rodgers CT, Krssak M, Andronesi OC, Trattnig S, Bogner W. Dynamic (31) P-MRSI using spiral spectroscopic imaging can map mitochondrial capacity in muscles of the human calf during plantar flexion exercise at 7 T. NMR Biomed 2016;29(12):1825–1834. [PubMed: 27862510]

126. Khegai O, Madelin G, Brown R, Parasoglou P. Dynamic phosphocreatine imaging with unlocalized pH assessment of the human lower leg muscle following exercise at 3T. Magn Reson Med 2018;79(2):974–980. [PubMed: 28560829]

127. Arnold DL, Matthews PM, Radda GK. Metabolic recovery after exercise and the assessment of mitochondrial function in vivo in human skeletal muscle by means of 31P NMR. Magn Reson Med 1984;1(3):307–315. [PubMed: 6571561]

128. Schmid AI, Schewzow K, Fiedler GB, Goluch S, Laistler E, Wolzt M, Moser E, Meyerspeer M. Exercising calf muscle T(2) * changes correlate with pH, PCr recovery and maximum oxidative phosphorylation. NMR Biomed 2014;27(5):553–560. [PubMed: 24610788]

129. Varghese J, Scandling D, Joshi R, Aneja A, Craft J, Raman SV, Rajagopalan S, Simonetti OP, Mihai G. Rapid assessment of quantitative T1, T2 and T2* in lower extremity muscles in response to maximal treadmill exercise. NMR Biomed 2015;28(8):998–1008. [PubMed: 26123219]

130. Weiss K, Schar M, Panjrath GS, Zhang Y, Sharma K, Bottomley PA, Golozar A, Steinberg A, Gerstenblith G, Russell SD, Weiss RG. Fatigability, Exercise Intolerance, and Abnormal Skeletal Muscle Energetics in Heart Failure. Circ Heart Fail 2017;10(7):e004129. [PubMed: 28705910]

131. Hoult DI, Busby SJ, Gadian DG, Radda GK, Richards RE, Seeley PJ. Observation of tissue metabolites using 31P nuclear magnetic resonance. Nature 1974;252(5481):285–287. [PubMed: 4431445]

132. Kemp GJ, Taylor DJ, Thompson CH, Hands LJ, Rajagopalan B, Styles P, Radda GK. Quantitative analysis by 31P magnetic resonance spectroscopy of abnormal mitochondrial oxidation in skeletal muscle during recovery from exercise. NMR Biomed 1993;6(5):302–310. [PubMed: 8268062]

133. Kemp GJ, Radda GK. Quantitative interpretation of bioenergetic data from 31P and 1H magnetic resonance spectroscopic studies of skeletal muscle: an analytical review. Magn Reson Q 1994;10(1):43–63. [PubMed: 8161485]

134. Beer M, Seyfarth T, Sandstede J, Landschutz W, Lipke C, Kostler H, von Kienlin M, Harre K, Hahn D, Neubauer S. Absolute concentrations of high-energy phosphate metabolites in normal, hypertrophied, and failing human myocardium measured noninvasively with (31)P-SLOOP magnetic resonance spectroscopy. J Am Coll Cardiol 2002;40(7):1267–1274. [PubMed: 12383574]

135. Tonson A, Ratel S, Le Fur Y, Vilmen C, Cozzone PJ, Bendahan D. Muscle energetics changes throughout maturation: a quantitative 31P-MRS analysis. J Appl Physiol (1985) 2010;109(6):1769–1778. [PubMed: 20847131]

136. Isbell DC, Berr SS, Toledano AY, Epstein FH, Meyer CH, Rogers WJ, Harthun NL, Hagspiel KD, Weltman A, Kramer CM. Delayed calf muscle phosphocreatine recovery after exercise identifies peripheral arterial disease. J Am Coll Cardiol 2006;47(11):2289–2295. [PubMed: 16750698]

137. Schur GM, Dunn J, Nguyen S, Dedio A, Wade K, Tamaroff J, Mitta N, Wilson N, Reddy R, Lynch DR, McCormack SE. In vivo assessment of OXPHOS capacity using 3 T CrCEST MRI in Friedreich's ataxia. J Neurol 2021.

138. Windschuh J, Zaiss M, Meissner JE, Paech D, Radbruch A, Ladd ME, Bachert P. Correction of B1-inhomogeneities for relaxation-compensated CEST imaging at 7 T. NMR Biomed 2015;28(5):529–537. [PubMed: 25788155]

139. Rerich E, Zaiss M, Korzowski A, Ladd ME, Bachert P. Relaxation-compensated CEST-MRI at 7 T for mapping of creatine content and pH--preliminary application in human muscle tissue in vivo. NMR Biomed 2015;28(11):1402–1412. [PubMed: 26374674]

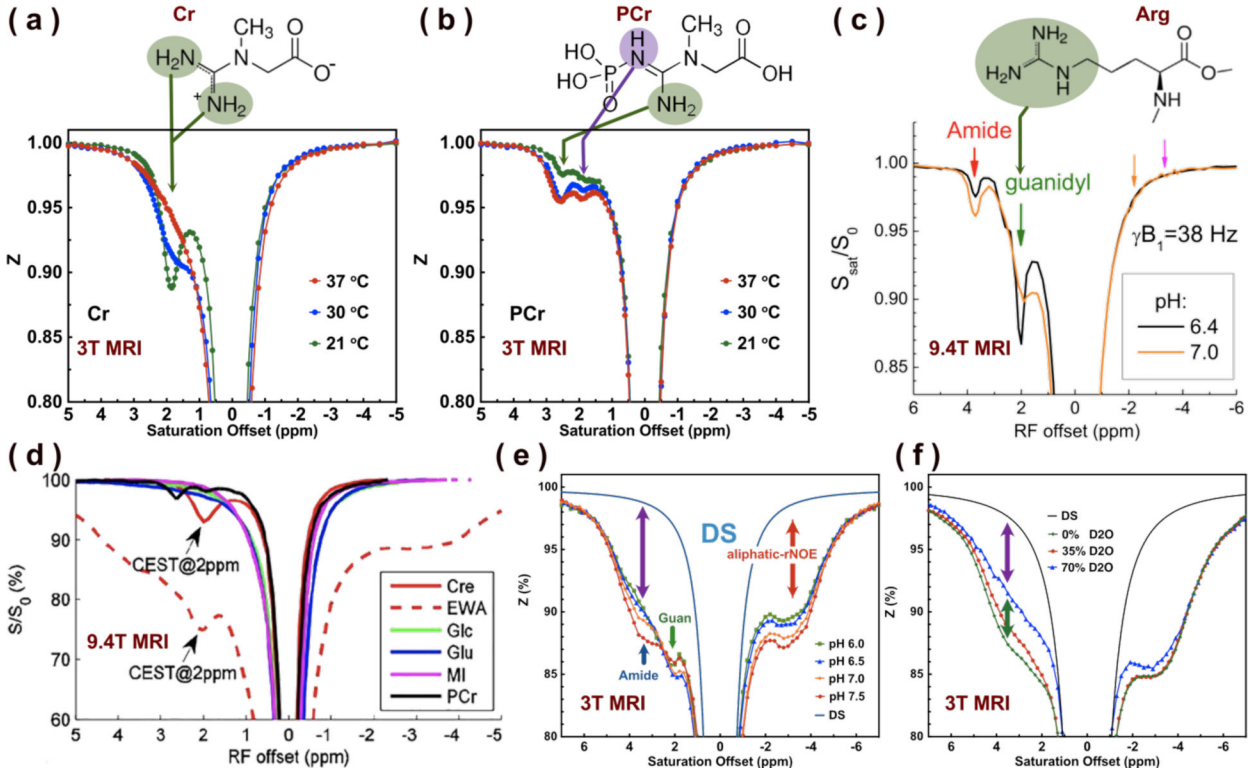

Figure 1.

Full Z-spectra of (a) creatine (Cr) and (b) phosphocreatine (PCr) phantoms with pH of 7.3 were measured with continuous wave (cw) CEST sequences and B_1 = 0.6 μT at three different temperatures using 3T MRI. The corresponding PCr and Cr molecular structures are plotted at the top of each figure together with the CEST peak assignments. Fig. a and b are modified from Chen L et. al., Nat Commun 2020; 11:1072. (c) Full Z-spectra of protamine phantoms with pH of 6.4 and 7.0 were measured with a cwCEST sequence and B_1 = 0.9 μT at 37 °C. The CEST signal from amide (red arrow) and arginine (Arg, green arrow) protons has opposite changes between the two pH phantoms. The molecular structure of the Arg residue in the proteins and peptides is depicted at the top of the figure. This figure is modified from Jin T et. al., NeuroImage 2017; 157: 341–350. (d) Full Z-spectra of Cr, egg white albumin, glutamate, glucose, myoinositol, and PCr were measured with a cwCEST sequence and B_1 = 1.0 μT at pH of 7.0 and 37 °C using 9.4T MRI. This figure is reprinted from Zhang XY et. al., Magn Reson Med 2017; 78: 881–887. (e) Z-spectrum of egg white as a function of pH with peak B_1 = 0.8 μT using a UTE-CEST sequence. The exchangeable protons downfield, amide and Arg, and AliphaticNOE signals are indicated. The simulated DS spectrum is also plotted. (f) The Z-spectra of egg white solution with 0% (green), 35% (red), and 70% (blue) D_2O acquired with ultrashort TE CEST with peak B_1 = 0.8 μT. A residual signal is still observable in the exchangeable proton range for 70% D_2O (purple arrow). Figures e and f are reprinted from Sui R et. al., Magn. Reson. Med. 2021; 86: 893–906.

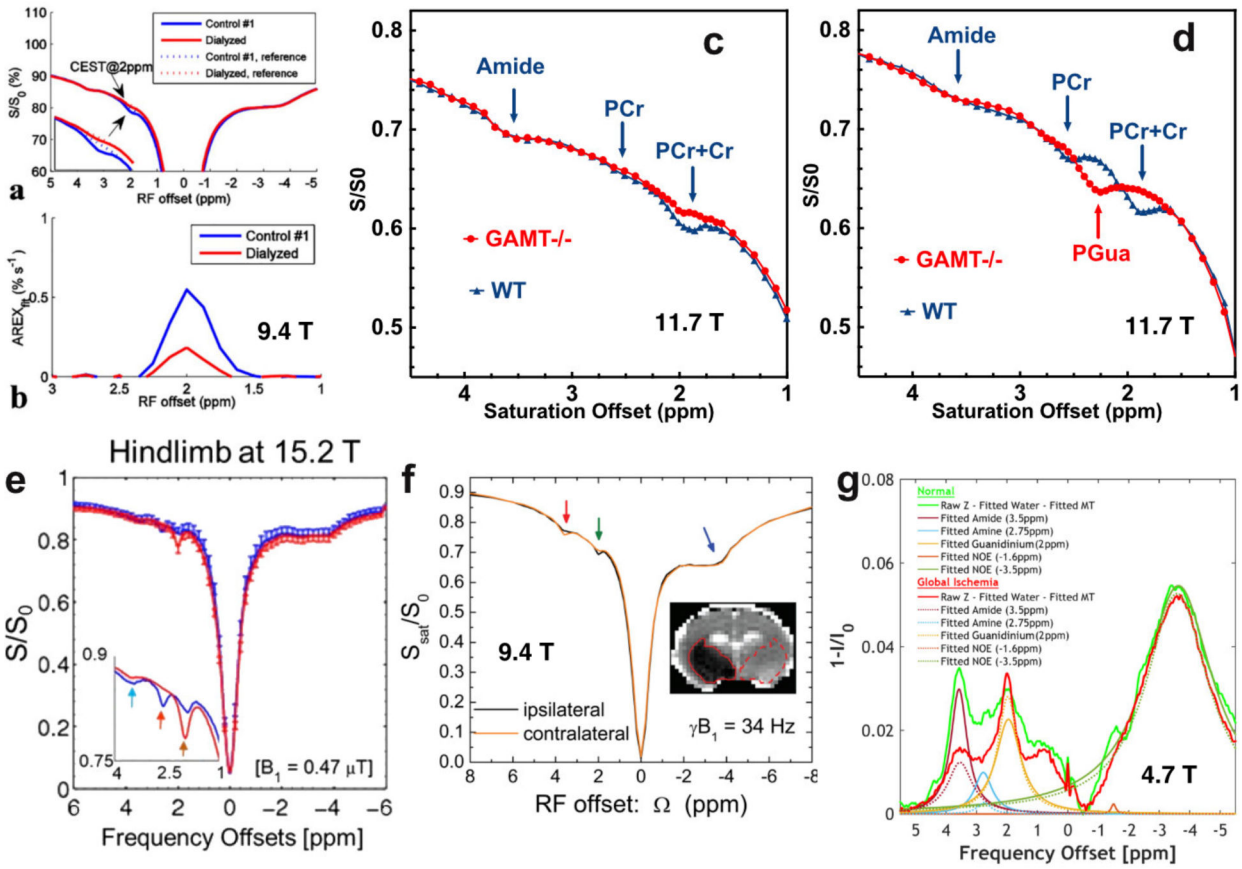

Figure 2.

(a) Full Z-spectra of rate brain homogenates (blue) and dialyzed brain homogenates (red), respectively with continuous wave CEST sequence and B_1 = 1 μT using 9.4T MRI. (b) The extracted CrCEST signal represented in apparent exchange dependent relaxation from rat brain homogenates with and without dialysis. Figs. a and b are preprinted from Zhang XY et. al., Magn Reson Med 2017; 78: 881. The averaged Z-spectra of (c) brain and (d) muscle for wild type and GAMT deficient mice at 11.7 T MRI. Figs. c and d were reprinted from Chen L et. al., NMR Biomed 2017; 30: e3834 and Chen L et. al., Magn Reson Med 2019; 81: 69, respectively. (e) The averaged Z-spectra (n = 6) of the mouse hindlimb before and after euthanasia with continuous wave CEST sequence and B_1 = 0.47 μT using 15.2T MRI. Fig.e was reprinted from Chung JJ et. al., Magn Reson Med 2019; 81: 3476. (f) Z-spectra with a saturation power of 0.8 μT were obtained from rat brains in the normal and ischemic region (n = 4) at 9.4 T MRI. The ipsilateral (solid) and contralateral (dashed) ROIs were selected based on the apparent diffusion coefficient (ADC) map (Inset). This figure was reprinted from Jin T et. al., NeuroImage 2017; 157:341. (g) A multipool Lorentzian fitting of the Z-spectra (B_1 = 0.75 μT) before (solid lines) and after global ischemia (dotted lines) show the contributions from different pools, including amideCEST (3.5 ppm), amineCEST (2.75 ppm), GuanCEST (2.0 ppm), NOE (−1.6 ppm), NOE (−3.5 ppm), as well as DS and MTC at 4.7 T. The fitted water and MTC effects were subtracted from the raw Z-spectra, showing apparent CEST contrasts between normal and ischemic tissues at amide (3.5 ppm),

amine (2.75 ppm), and guanidinium (2.0 ppm) offsets. This figure was reprinted from Zhou IY et. al., Magn Reson Med 2019; 81: 645.

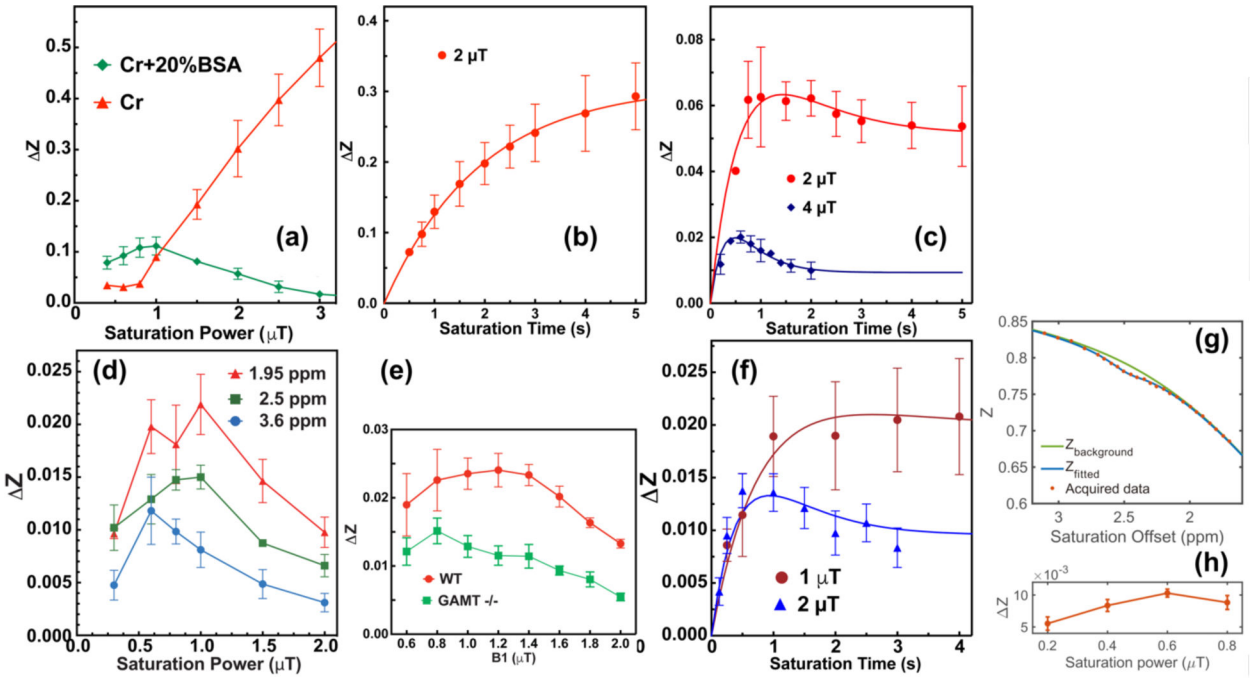

Figure 3.

(a) A schematic representation of brain Z-spectrum with typical contributions including DS, MTC, amideNOE, aromaticNOE, aliphaticNOE, amideCEST, CrCEST, PCrCEST, hydroxylCEST and amineCEST. The DS component is also included in the amineCEST and hyroxylCEST lineshapes. Here, the DS is plotted for reference only. The zoomed CEST contributions are plotted in the Figs. b-e. (b) The nonCEST saturation transfer processes that contribute to the brain Z-spectrum, e.g. amideNOE, aromaticNOE, aliphaticNOE and MTC. MTC is a strong and broad signal with center at around −3.5 to −3 ppm. Amide and aromatic NOE peaks distribute between 2 to 5 ppm, while aliphaticNOE centers at −3.5 to −3 ppm. (c) The CEST signals from the protons with slow to intermediate exchange rates, e.g. ArgCEST and CrCEST at 2 ppm, amideCEST at 3.5 ppm and PCrCEST at both 2 ppm and 2.5–2.6 ppm. Here amideCEST is used to distinguish from APT that is usually obtained by asymmetry analysis. (d) The peak locations of the amine protons from glutamate (3 ppm) and protein (2.7 ppm), as well as hydroxyl protons (1 ppm) from both protein and metabolites (e.g. myoinositol, glucose and glucogen). (e) The amine and hydroxyl CEST signal that coalescence with water peak due to higher exchange rates (>1000 s^{-1}). The water peak (DS) is also plotted in both Figs. d and e for comparison.

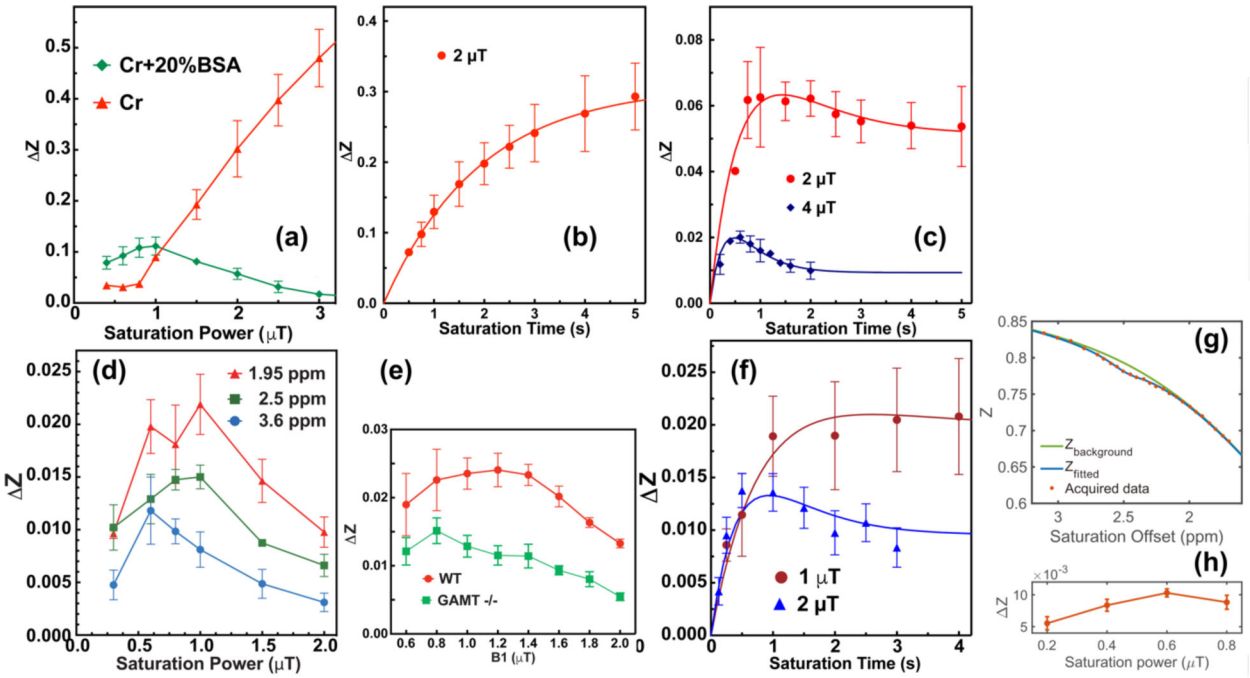

Figure 4.

(a) The CrCEST signal of Cr solution (50 mM) and Cr (50 mM) mixed with 20% cross-linked BSA as a function of saturation power with a fixed saturation length of 5s at 11.7T. The CrCEST was extracted by the polynomial and Lorentzian line-shape fitting (PLOF) method. (b) The saturation length dependent CrCEST signal of the Cr phantom (50 mM) for a saturation power of 2 μT. (c) The saturation length dependent CrCEST signal of the Cr (50 mM) mixed 20% cross-linked BSA phantom for saturation powers of 2 μT and 4 μT, respectively. (d) Observed CEST signals (ΔZ) at 3.6 ppm, 2.5 ppm, and 2 ppm as a function of saturation power for the mouse hindleg at 11.7T with a fixed saturation time of 2 s. Fig. d was reprinted from Chen L et. al., Magn Reson Med 2019; 81:69. (e) The observed CEST at 2 ppm with respect to the saturation power for the mouse brain of wild type and guanidinoacetate N-methyltransferase-deficient mice. Fig. e was reprinted from Chen L et. al., NMR Biomed 2017; 30: e3834. (f) The observed CEST signal at 2 ppm as a function of saturation time over the whole mouse brain for saturation powers of 1 μT and 2 μT, respectively. In all the above figures, the CEST signals were extracted with the PLOF method. Figs. g and h were reprinted from Chen L et. al., Nat Commun 2020;11(1):1072. Figs. a, b, c and f were reprinted from Chen L et. al., NMR Biomed 2019; 32: e4168.

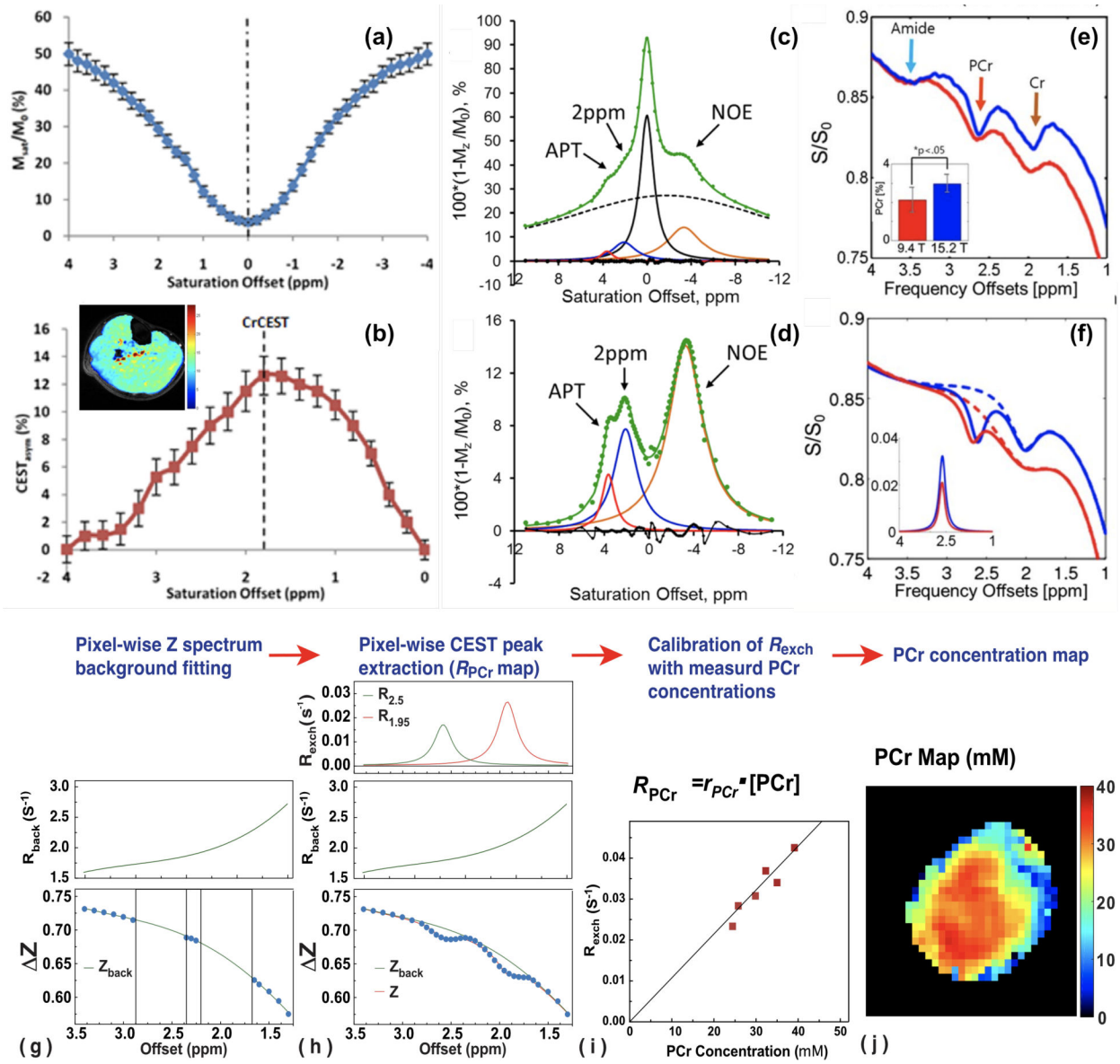

Figure 5.

(a) The z-spectra and (b) corresponding asymmetry plots for the soleus muscle at baseline at 7T. Insert figure is a CrCEST asymmetry map. Here the signal (S(1.8)-S(−1.8)) was divided by S(−1.8) instead of S_0. Figs. a and b were reprinted from Kogan F et. al., Magn Reson Med 2014; 71:164. (c) Z-spectra of a wild type mouse brain fitted with Lorentzian functions using five pools. (d) Water DS and MTC were subtracted from the Z-spectra to extract amideCEST, GuanCEST and aliphaticNOE. Figs. c and d were reprinted from Cai K et. al., NMR Biomed 2015; 28: 1. (e) Averaged Z-spectra of the mouse hindlimb collected at two different MRI fields (9.4T and 15.2T). The statistical comparison of PCrCEST from local Lorentzian fitting for the two fields are compared. (blue bar: 15.2T; red bar: 9.4 T) (f) Local Lorentzian fit to extract PCrCEST for two fields (blue line: 15.2T; red line: 9.4 T). The background lines for the fitting are plotted in dashed lines. Figs. e and f were reprinted from Chung JJ et. al., Magn Reson Med 2019; 81:3476. (g-j) Flowchart of the polynomial

and Lorentzian line-shape fitting (PLOF) method for PCr mapping. (g) First, pixel-wise background Z-spectrum $Z(R_{back})$ is fitted using data points from outside the range of the CEST peaks using Eqs.2, 3 and 6. (h) Pixel-wise R_{exch} values are obtained by fitting the full Z-spectrum $Z(R_{back} + R_{exch})$ with fixed R_{back} according to Eqs.2–4. (i) R_{exch} is calibrated using the metabolic concentrations measured by $^{31}P/^{1}H$ MRS. (j) The PCr concentration map of the mouse hind leg is calculated from the R_{exch} map after calibration.

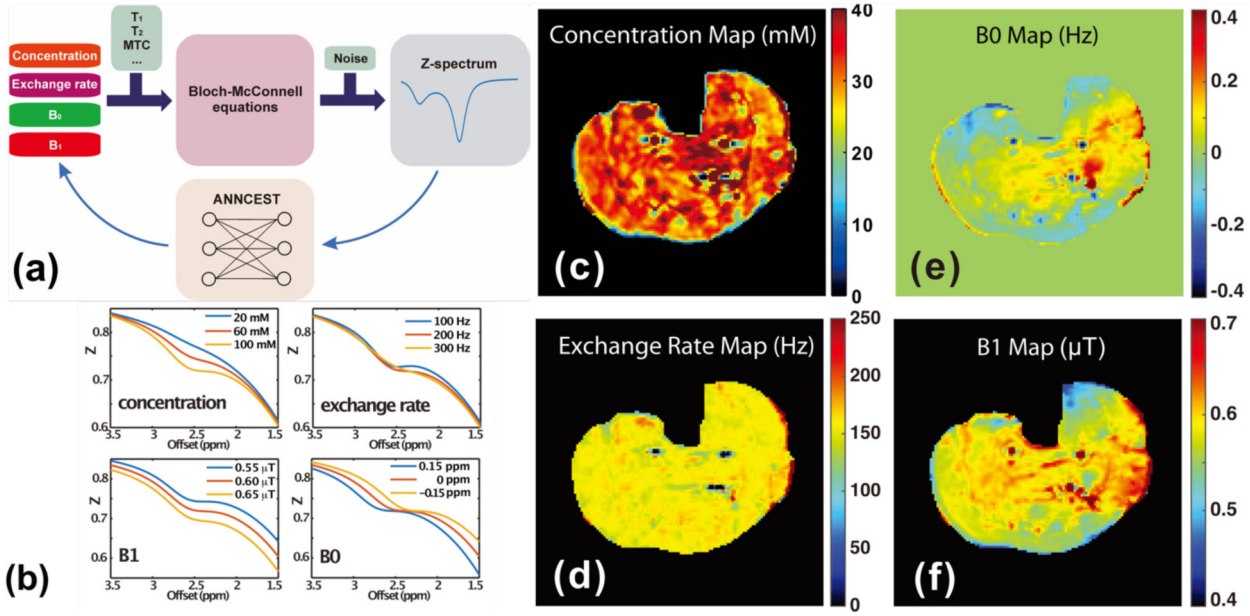

Figure 6.

(a) Schematic flowchart of ANNCEST. The annotated Z-spectra are simulated by Bloch-McConnell equations to mimic realistic tissue conditions by selecting proper parameters such as T_1, T_2, MTC, and noise. ANNCEST is trained to extract relevant features between the Z-spectrum and quantifiable parameters. (b) The simulated *in vivo* Z-spectra with one single peak (2.5 ppm) and one MTC background as a function of different concentrations, exchange rates, saturation powers and B_0 values. The typical PCr concentration (c) and exchange rate (d) maps together with the B_0 (e) and B_1 (f) maps obtained by the ANNCEST method on human skeletal muscle using the CEST images acquired with 0.6 μT saturation power and 0.8 s saturation length. All figures are reprinted from Chen L et. al., Nat Commun 2020; 11:1072.

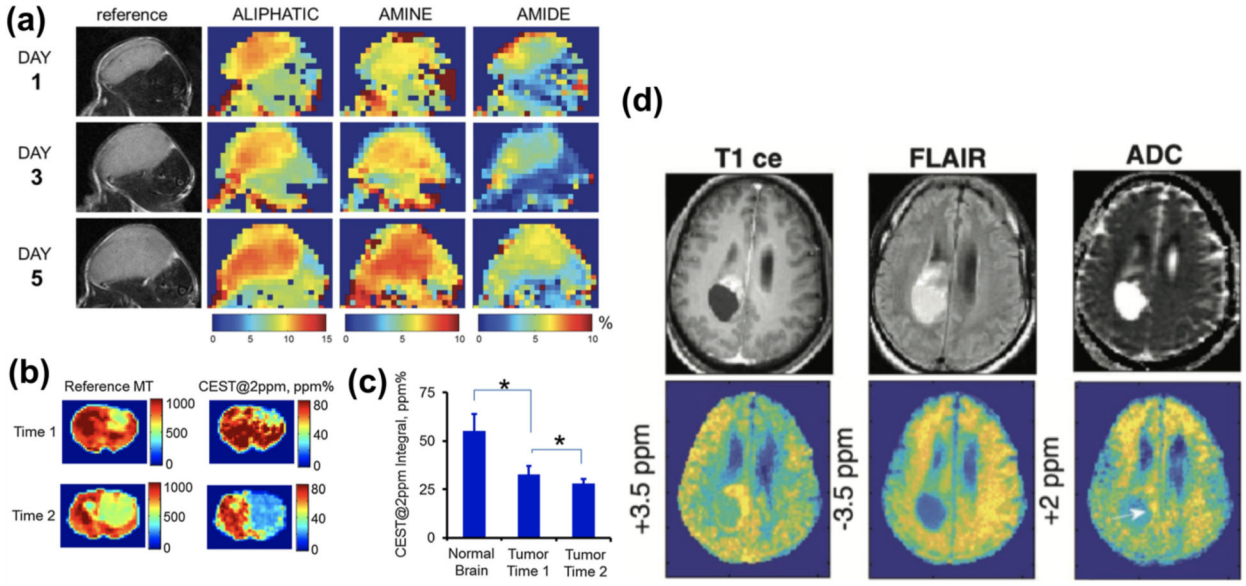

Figure 7.

(a) Lewis lung carcinoma tumor progression revealed by the AliphaticNOE, CEST(2 ppm) (denoted as amine in the paper), and CEST(3.5) (denoted as amide in the paper) maps on the hind leg of a typical animal followed over a 5-day period. Maps were produced from the Lorentzian fitting algorithm. This figure was reprinted from Desmond KL et. al., Magn Reson Med 2014; 71: 1841. (b-c) The CEST integral signal at 2 ppm decreased in tumor compared with normal brain tissue and further reduced with tumor progression. This figure was reprinted from Cai K et. al., NMR Biomed 2015; 28: 1. (d) Application of CEST at ± 3.5 ppm and 2 ppm to a human patent with brain tumor at 9.4 T. The enhancement at the edge of the cyst is visible in the 3.5 ppm CEST map, while the CEST at 2 ppm show different contrast from both contrast at ±3.5 ppm. This figure was reprinted from Zaiss M et. al., Magn Reson Med 2019; 81: 3901.

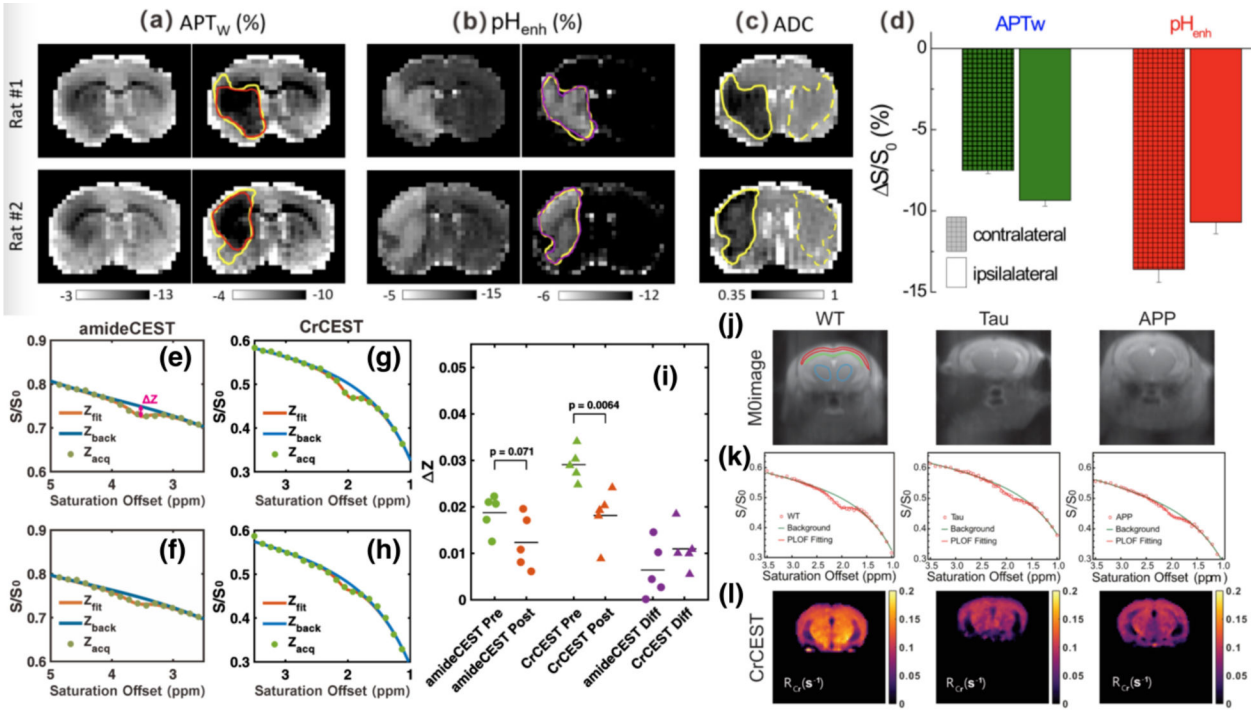

Figure 8.

(a) Comparison of in vivo APT weighted image (APTw) and pH enhance (pH_{enh}) maps on rat brain with stroke model. (a-b) APTw and pH_{enh} maps for two typical rat brains measured at 2 h post stroke are plotted with two different scale bars (10% and 6%). (c) Respective apparent diffusion coefficient maps showed the ischemic core region. (d) The magnitude of contrast between ipsilateral and contralateral ROIs, respectively. The pH_{enh} contrasts are higher than those for APTW. Figures a-d were reprinted from Jin T et. al., Neuroimage 2017; 157: 341. (e-i) Sensitivity of amideCEST and CrCEST MRI for detecting pH changes in mouse brain during CO_2 inhalation. Representative Z-spectra for amideCEST (e,f) and CrCEST (g,h) experiments (e,g) pre-CO_2 and (f,g) during CO_2 inhalation for the cortex region. Solid lines are the background fitted using the polynomial and Lorentzian line-shape fitting (PLOF) method. (i) Scatter plots showing the difference for amideCEST and CrCEST experiments extracted by PLOF (n= 5). (j-l) Typical S_0 images (j) cortical CrCEST Z-spectra (k), CrCEST maps (l) for wild type, Tau and APP AD mouse models. Both CrCEST Z-spectra and CrCEST maps of Tau and APP mice show a clear signal reduction compared to WT mice. Figures e-i were reprinted from Chen L et. al., NeuroImage 2021; 236: 118071.

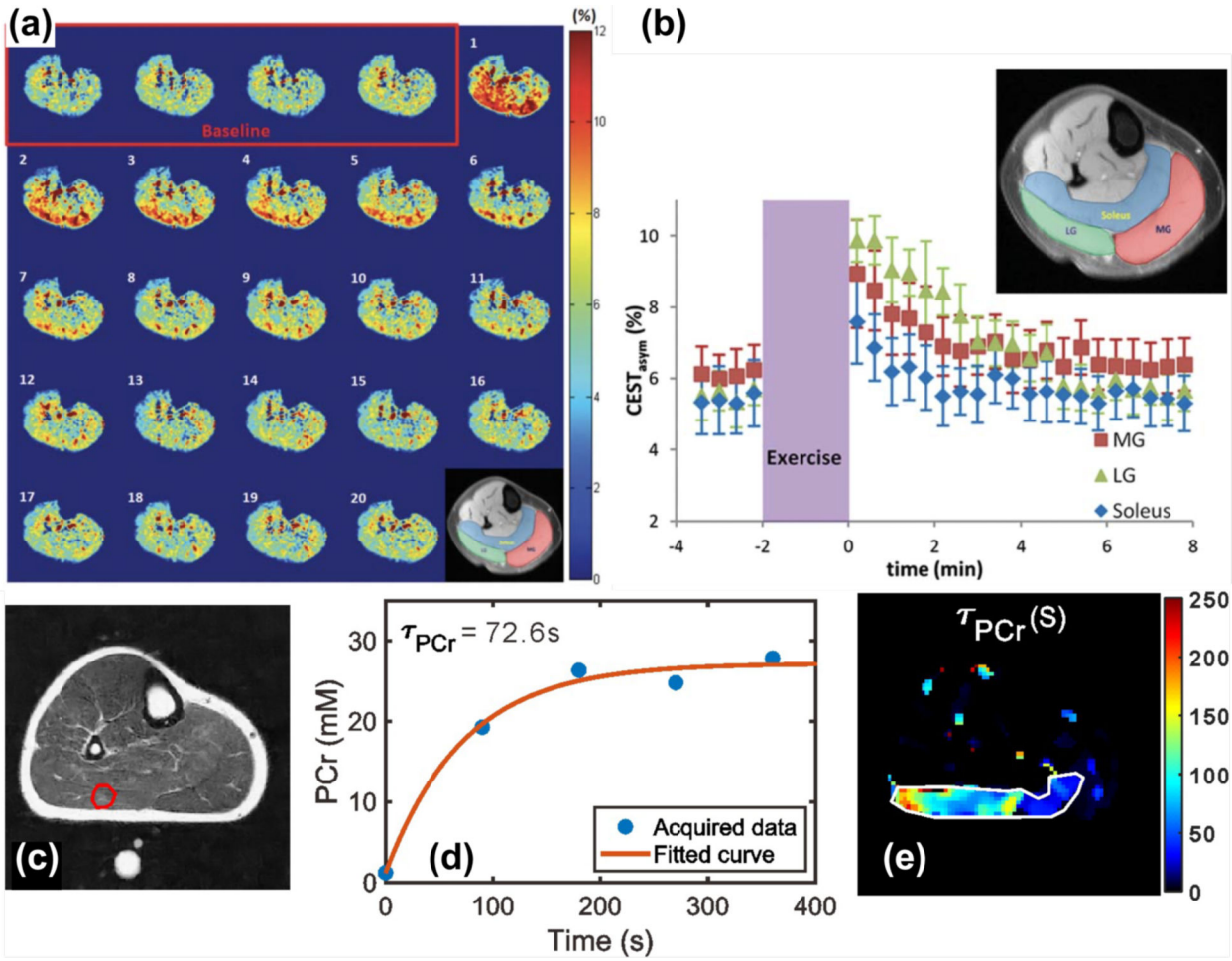

Figure 9.

(a) CrCEST maps of a human calf muscle extracted by asymmetry analysis are shown. Figs. a and b before and every 24 seconds after 2 minutes of mild plantar flexion exercise. The segmented anatomical image is displayed in the insert image. (b) The averaged CrCEST signal as a function of time in three different muscles of the calf from Fig. a. Figures a-b were reprinted from Kogan F et. al., J Magn Reson Imaging 2014; 40: 596. (c-e) Calculation of the PCr recovery time constant τ_{PCr} from the Cr maps measured with PCrCEST. (c) T_2 weighted anatomical image and selected ROI (red circle) for the following PCr measurement. (d) The PCr concentration as a function of recovery time and the fitting curve with a single exponential recovery function. (c) The typical τ_{PCr} map from the pixel-wise PCr fitting curve. The fitted τ_{PCr} values within the regions circumscribed by the white line are 70.7 ± 55.4 s (mean ± s.d.). Figures c-e were reprinted from Chen L et. al., Nat Commun 2020;11:1072.

Table 1:

Comparison of difference CEST quantification methods.

Quantification methods	Advantages	Disadvantages	Applications
MTasym	Easy to implement. Short scan time.	Many sources of contamination from MTC, other CEST/NOE contrasts and T_1/T_2.	Relative CEST signal change in tumor assessment, contrast agent injection and pH alternation. Glutamate and CrCEST change during challenging.
Lorentzian fitting	Suppressing MTC, DS and T_1/T_2 contamination. Achieving multiple CEST contrasts in one scan.	Long scan time. Still has contaminationfrom other CEST/NOE contrasts.	Protein profiling in tumor assessment and neurodegenerative diseases.
PLOF	Highly specific.	Only works for CEST contrasts with distinguishable peaks. Scan time is longer than MTasym but shorter than Lorentzian fitting	Quantification of amideCEST, CrCEST, PCrCEST and ArgCEST.
Three-point Method	Highly specific. Short scan time	Only works for CEST contrasts with distinguishable peaks and the peaks must be far away from water. Requires perfect shimming.	Relative CEST signal change in amideCEST and CrCEST at high fields.
ANNCEST	Highly specific. Short processing time once ANN is well trained.	ANN network training is challenging. Scan time is longer than MTasym but shorter than Lorentzian fitting	Quantification of amideCEST, CrCEST, PCrCEST and ArgCEST.